Targeting ATM enhances radiation sensitivity of colorectal cancer by potentiating radiation-induced cell death and antitumor immunity

Yuwen Xie [a,b,1], Yang Liu [a,1], Mingdao Lin [c,1], Zhenkang Li [d], Zhiyong Shen [e], Shengqi Yin [a], Yilin Zheng [a], Yishu Zou [a], Yaowei Zhang [a], Yizhi Zhan [e,*], Yuan Fang [a,*], Yi Ding [a,*]

[a] Department of Radiation Oncology, Nanfang Hospital, Southern Medical University, Guangzhou 510515, Guangdong, China
[b] Department of Radiation Oncology, Hainan General Hospital, Hainan Affiliated Hospital of Hainan Medical University, Haikou 570311, Hainan, China
[c] Department of Anorectal Surgery, Hainan General Hospital, Hainan Affiliated Hospital of Hainan Medical University, Haikou 570311, Hainan, China
[d] Department of Surgery, Zhujiang Hospital, Southern Medical University Guangzhou 510280, Guangdong, China
[e] Department of General Surgery & Guangdong Provincial Key Laboratory of Precision Medicine for Gastrointestinal Tumor, Nanfang Hospital, The First School of Clinical Medicine, Southern Medical University, Guangzhou 510515, Guangdong, China

HIGHLIGHTS

- High ATM phosphorylation correlates with poor radiotherapy response in patients with colorectal cancer.
- ATM inhibition amplifies radiation-induced ROS accumulation and mitochondrial damage, activating the STING pathway.
- The combination of radiotherapy and ATM inhibition boosts CD8+ T cell recruitment and activation.
- ATM inhibition mitigates radiation-induced PD-L1 upregulation via the NEMO/NF-κB pathway, enhancing immune responses.
- A novel combination of radiotherapy, ATM inhibitor, and PD-L1 blockade enhances tumor regression and survival.

GRAPHICAL ABSTRACT

Proposed working model of targeting ATM for enhancing the radiation sensitivity of colorectal cancer. Targeting ATM increased IR-induced ROS levels, which not only triggers apoptosis but also aggravates mitochondrial damage, and facilitates cytosolic mtDNA-induced STING type-I IFN signaling. Activation of this pathway enhances the overall radiation response by boosting antitumor immune responses, thereby improving the effectiveness of radiation therapy in treating CRC.
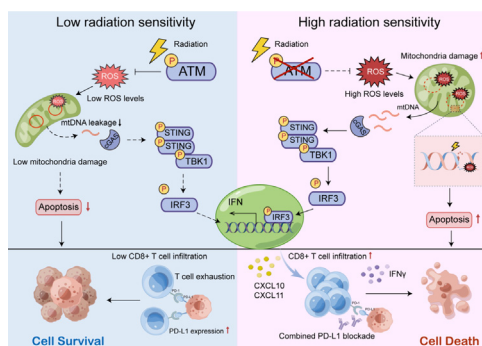
ARTICLE INFO

ABSTRACT

Introduction: The efficacy of radiotherapy in colorectal cancer (CRC) is often limited by radiation resistance. Ataxia telangiectasia mutated (ATM) is well known for its role in repairing double-strand DNA breaks within the DNA damage response (DDR) pathway. However, whether ATM mediates other mechanisms contributing to radiation resistance remains insufficiently investigated.
Objectives: This study investigates how targeting ATM enhances CRC radiation sensitivity and evaluates combination strategies to improve radiotherapy outcomes.
Methods: Clinical specimens were analyzed to correlate ATM activation with radiotherapy response. Functional assays, including EdU, cell viability, clonogenic survival, and apoptosis assays, were used to assess the impact of ATM inhibition on radiation sensitivity. Mechanistic insights were gained through

---

* Corresponding authors at: Nanfang Hospital, Southern Medical University, No.1838, North Guangzhou Avenue, Baiyun District, Guangzhou, Guangdong, China, 510515.
  E-mail addresses: yizhi2012@smu.edu.cn (Y. Zhan), fangyuan1313@163.com (Y. Fang), dingyi197980@126.com (Y. Ding).
  [1] Yuwen Xie, Yang Liu, Mingdao Lin contributed equally to this work.

STING pathway
Combination strategies

RNA-seq, RT-qPCR, western blotting, ELISA, immunofluorescence, flow cytometry, ChIP-qPCR, and co-immunoprecipitation. In vivo efficacy was evaluated using subcutaneous tumor models in nude, BALB/c, and C57BL/6J mice.

Results: High ATM phosphorylation levels correlated with poor radiotherapy response in CRC patients. ATM inhibition enhanced radiation sensitivity in both in vitro and in vivo models. Mechanistically, ATM inhibition increased radiation-induced ROS accumulation and mitochondrial damage, leading to the release of mitochondrial DNA (mtDNA) into the cytosol and activation of the STING-type I interferon pathway. This enhanced CD8+ T cell infiltration and boosted antitumor immunity. Additionally, ATM inhibition partially alleviated the radiation-induced upregulation of PD-L1, likely through the ATM/NEMO/NF-κB pathway. Notably, triple therapy combining radiotherapy, an ATM inhibitor, and anti-PD-L1 achieved superior tumor control and remission in mouse models, including large, treatment-resistant tumors.

Conclusion: Targeting ATM enhances radiation-induced tumor cell death and boosts antitumor immune responses, offering a promising strategy to overcome CRC radiation resistance. The synergy of radiotherapy, ATM inhibitor, and immune checkpoint blockade highlights a novel therapeutic approach for CRC management.

Introduction

Colorectal cancer (CRC) remains one of the leading causes of cancer-related morbidity and mortality worldwide [1]. Radiotherapy (RT) is a cornerstone in the treatment of locally advanced rectal cancer and serves as a palliative option for advanced CRC. However, the efficacy of RT is often limited by tumor resistance to ionizing radiation (IR) [2]. A critical factor in this resistance is the activation of DNA damage response (DDR) pathways, which repair DNA damage to maintain cellular viability and genomic stability upon IR exposure [3]. Central to these pathways is the Ataxia telangiectasia mutated (ATM) protein, a serine/threonine kinase encoded by the ATM gene. ATM becomes activated through autophosphorylation at Ser1981 upon DNA double-strand breaks, initiating a phosphorylation cascade that leads to DNA repair and cell cycle checkpoint responses [4]. ATM is well-known for its role in repairing double-strand DNA breaks. However, its additional functions and interactions with other signaling pathways after radiation activation remain areas for further exploration.

The effectiveness of radiation is influenced not only by direct DNA damage but also by the generation of reactive oxygen species (ROS), which contribute to indirect DNA damage [6]. Despite growing interest, the impact of ATM inhibition on ROS levels and mitochondrial function in CRC remains unclear. Beyond cellular damage, radiation can also activate antitumor immunity through multiple mechanisms. Targeting DDR pathways has emerged as a promising strategy to enhance these immune responses, with DDR inhibitors like PARP and ATR inhibitors showing potential in combination with RT [7]. However, unlike inhibitors targeting other DDR components, ATM inhibitors have not yet reached late-stage clinical trials, highlighting their substantial research potential. The potential of AZD0156, a selective oral ATM inhibitor [5], to enhance radiotherapy response and its underlying antitumor mechanisms warrant further exploration.

While radiotherapy can activate immune responses, it can also upregulate PD-L1 expression through various signaling pathways [8]. The upregulation of PD-L1 may suppress antitumor immunity, potentially contributing to suboptimal therapeutic outcomes of RT. Whether radiation-induced activation of ATM regulates PD-L1 expression in tumor cells remains to be clarified.

In this study, we explored the relationship between ATM activation and radiotherapy response in CRC. Using gene editing and the ATM inhibitor AZD0156, we demonstrated that ATM inhibition significantly enhances radiation sensitivity both in vitro and in vivo. We propose that AZD0156 amplifies radiation-induced accumulation of ROS and mitochondrial dysfunction, resulting in the release of mitochondrial DNA (mtDNA) into the cytoplasm. This cytoplasmic mtDNA activates the STING-type I interferon pathway, thereby boosting antitumor immunity. Additionally, we found that radiation-induced activation of the ATM/NEMO/NF-κB pathway upregulates PD-L1 expression. Based on these findings, we present a novel triple therapy combining radiotherapy, ATM inhibitior, and PD-L1 blockade, which achieves effective tumor control and complete remission in mouse models, including large and treatment-resistant tumors. This approach offers a promising strategy to overcome CRC resistance to radiotherapy and improve clinical outcomes.

Material and methods

Xenograft and allograft mouse models

For the xenograft model, female BALB/c-nu/nu mice (4–6 weeks old) were provided by Guangdong Medical Laboratory Animal Center. Human HCT116, SW480 and SW620 CRC cells (5×10^6) were subcutaneously planted in the back of mice. BALB/c mice or C57BL/6 mice (4–6 weeks old) were provided by the Southern Medical University Animal Center or Guangdong Medical Laboratory Animal Center. Murine MC38 CRC cells (1×10^6) were subcutaneously planted in the back of C57BL/6 mice and murine CT26 CRC cells (1×10^6) were subcutaneously planted in the back of BALB/c mice. When tumors reached the required size for the experiment, mice were randomized into various treatment groups. Tumors volumes were calculated by formula: length*width*height/2 (mm^3). Mice were sacrificed when the tumor diameter reached 20 mm or when the tumor size reached 2000 mm^2. The end point was designated as 4 weeks after the first radiation. The formula for tumor growth rate is: (V-V0) / V0*100 %, V = Final volume at endpoint, V0 = Volume before radiotherapy.

Mice treatments

Mice received ionizing radiation on days 1, 3 and 5 from the start of treatment using a linear accelerator (Varian Clinac 23EX Linear Accelerator) in the Department of Radiation Oncology at Nanfang Hospital. Mice were given AZD0156 (Selleck, S8375) with 10 mg/kg by gavage at least one hour prior to radiation treatment. Mice in the blank control group were given PSB treatment. For STING inhibitor experiment, mice were injected intraperitoneally with C-176 (Med Chem Express, HY-112906; 5 mg/kg) every other day. C-176 treatment began in one week before IR and ended one week after IR. For the PD-L1 blockade experiment, one day after

radiation, anti-mouse PD-L1 (BioXcell, BE101) was delivered intraperitoneally at 200 ug/mouse.

Cell lines

All CRC cell lines were obtained from Guangdong Provincial Key Laboratory of Molecular Tumor Pathology. Cells were cultured with RPMI1640 medium (Gibco, USA) in 37℃, 5 % CO_2 incubator. All cell lines were supplemented with 10 % fetal bovine serum (Gibco, USA).

Western blot analysis

Western blot analysis was performed according to standard methods as described previously [9]. Protein lysates of cells or tissues were prepared by RIPA Lysis Buffer (Beyotime, China) containing protease and phosphatase inhibitor cocktail (CWBIO, China). Protein concentrations were determined by NanoDrop (Thermofisher, USA). The primary antibodies and concentrations used are as follows: Anti-Alpha Tublin (1:1000, proteintech, 11224–1-AP); Anti-GAPDH (1:1000, proteintech, 10494–1-AP); Anti-phospho-ATM (Ser1981) (1:500, Bioss, bsm-54103R); Anti-ATM (1:1000, Abclonal, A1965); Anti-cGAS (1:1000, Abclonal, A8335); Anti-STING (1:1000, Abclonal, A21051); Anti-Phospho-STING-S365 (1:1000, Abclonal, AP1199); Anti-TBK1/NAK (1:1000, Abclonal, A3458); Anti-Phospho-TBK1/NAK-S172 (1:1000, Abclonal, AP1026); Anti-IRF3 (1:1000, Abclonal, A19717); Anti-Phospho-IRF3-S396 (1:1000, Abclonal, AP0623); Anti-Phospho-STAT1-Y701 (1:1000, Abclonal, AP0054); Chk2 (1:2000, ABclonal, A19543), Anti-Phospho-Chk2-T68 (1:1000, ABclonal, AP0590), Anti-Beclin1 (1:2000, ABclonal, A21191), Anti-Phospho-Beclin1-Ser90 (1:100, ABclonal, AP1254), Anti-MAP1LC3A (1:1000, ABclonal, A12319), Anti-PD-L1/CD274 (1:1000, proteintech, 66248–1-Ig), Anti-NF-κB p65 (1:1000, CST, 8242 T), Anti-Phospho-NF-κB p65 (Ser536) (1:1000, CST, 3033 T). The second antibody and concentrations used is as follows: Goat Anti-Rabbit IgG (H + L) (1:2000, DIA-AN, Q1002), HRP-conjugated Goat anti-Mouse IgG (H+L) (1:2000, ABclonal, AS003). Proteins were detected using ECL luminous fluid (Tanon, China) and images were captured using the Tanon Imaging System. Image J software was uesd for protein quantification.

Stable cell line construction

Lentiviral vectors plasmids was purchased from VigeneBio (Shandong, China). shRNA (shATM) or short hairpin RNA (shNC) were transfected into SW480 and SW620 cells to construct the stable ATM knockdown cell lines. The transfection steps were performed according to provided protocols. Briefly, cells were plated in 24-well plates and lentiviruses infection was performed when the cell density reached around 70–80 %. Cells were incubated with serum-free RPMI1640 medium for 24 h. Then, cells were selected with puromycin for 7 days and expanded. Knockdown efficiency was assessed by western blot.

Immunohistochemistry (IHC)

IHC staining was performed according to standard methods as described previously [9]. Briefly, tissue sections were deparaffinized, rehydrated, subjected to antigen retrieval, and incubated with primary antibodies overnight at 4℃. The primary antibodies and concentrations used are as follows: Anti-Phospho-ATM (S1981) (1:100, R&D Systems, AF1655); Anti-Ki67 (1:800, CST, 9449); Anti-CD8α (1:600, abcam, ab209775). The second antibody was purchased from ZSGB-BIO (PV-600). The IHC score was obtained as the product of percentage and intensity of staining. The percentage of positive cells was scored as follows: 0, no posi-

tive cells; 1, $\leq$25 % positive area; 2, 26–50 % positive area; 3, 51–75 % positive area and 4, $>$75 % positive area. The staining intensity was scored as follows: 0, no staining; 1, weak staining intensity; 2, moderate staining intensity; and 3, strong staining intensity. The tissue sections were counted or analyzed under 40 × magnification. Five fields of vision were randomly selected and the average was calculated.

5-Ethynyl-2′-deoxyuridine (Edu) assay

EdU assays were performed using the EdU Cell Proliferation Assay Kit (RIBOBIO, China). SW620 or SW480 cells were planted in 96-well plates with 3000 cells/well. After cells had adhered to the wall (overnight), AZD0156 were added into each well and then were exposed to IR at a dosage of 6 Gy. Medium was replaced with new RPMI1640 medium 24 h later. Cell culture was terminated 72 h after IR. The EdU assay procedure was based on the instruction manuals. The stained cells were observed under the microscope (Olympus, Japan).

Cell counting kit-8 (CCK-8)

For cell viability assays, cells were seeded at a density of 1000–2000 cells per well on 96-well plates. After cells had adhered to the wall (overnight), different concentrations of AZD0156 were added into each well and then were exposed to IR at a dosage of 6 Gy. Medium was replaced with new RPMI1640 or DMEM medium 24 h later. Cell culture was terminated 48-72 h after IR. Cell viability were detected with cell counting kit-8 (DOJINDO Laboratories, Japan) at 450 nm.

Radiation colony formation assay

Cells were seeded into 6-well plates at a density of 1000, 2000, 4000, 6000 and exposed to IR at a dosage of 0, 2, 4, 6 doses, respectively. AZD0156 were added into each well and then were exposed to IR at various dosages. Medium was replaced with new RPMI1640 or DMEM medium 24 h later. Incubation was stopped after 10 to 14 days. Subsequently, cells were fixed with methanol for 15 min and stained with crystal violet solution for 30 min. The image was taken by gel imager (Bio-Rad) and Image J software was used to calculate the clone numbers. Plating efficiency (PE) was used to calculate the survival fraction (SF). PE= (number of clones / number of seed cells) × 100 %. SF = (PE of X Gy) / (PE of 0 Gy). The curves were fitted using the Graphad Prism 9.0 software based on Linear-Quardratic (L-Q) Formulation: SF = e-D(α + βD). The radiobiological parameters were obtained by the single-hit multi-target model: SF = 1-(1-e-D/D0) N.

Flow cytometry of ROS and JC-1

Intracellular ROS and mitochondrial ROS were measured by flow cytometry. Intracellular ROS levels were detected using the DCFH-DA fluorescent probe (UElandy, R6033), and mitochondrial ROS levels were measured with MitoSOX Red reagent (MedChemExpress, HY-D1055). Both probes were diluted in serum-free medium following the kit instructions. 24 h after radiation, cells were incubated with the diluted DCFH-DA solution at 37℃ in the dark for 1 h. Cells were then washed twice with serum-free medium to remove uninternalized DCFH-DA or MitoSOX Red reagent. ROS and mtROS fluorescence intensity was analyzed by flow cytometry. Mitochondrial membrane potential changes were assessed using the JC-1 Mitochondrial Membrane Potential Assay Kit (Solarbio, CA1310-100). The experiment was conducted 24 h after radiation and AZD0156 treatment, following the protocol provided by the kit.

Transmission electron microscopy

The cells were planted in a dish at 1×10^6 cells/dish for 24 h. After the addition of AZD0156, radiation treatment was performed. Cells were harvested 24 h post-radiation in a 1.5 ml EP tube and then were washed twice in PBS. After centrifugation, the supernatant was discarded, and 2.5 % glutaraldehyde was slowly added along the wall to fix the cells. Electron microscopic analysis of samples was performed at the KingMed Company (Guangzhou, China).

Quantification of cytosolic mtDNA

Cells were permeabilized for 10 min with digitonin buffer (150 mM NaCl (Biosharp, BL542A) + 50 mM HEPES (Beyotime, C0217) + 25 μg/ml digitonin (Beyotime, ST1272)) according to the method reported [10]. The solution was centrifuged at 16,000 g for 25 min at 4℃. A 1:15 dilution of the supernatant was used for qPCR to detect the MTATP8 and GAPDH expression. The pellet was used for the extraction of total DNA with the TIANamp Micro DNA Kit (TIANGEN Biotech). The amount of cytosolic mtDNA in the supernatant was normalised to the amount of total mtDNA in the pellet.

RNA sequencing

RNA-Seq was performed to compare the transcriptome profiles of the IR treatment and IR plus AZD0156 treatment tumors grown in BALB/c mice, which were harvested on day 14 after radiation. RNA-seq was performed by Applied Protein Technology (Shanghai, China). All the samples were sequenced on an Illumina Novaseq 6000 (or MGISEQ-T7) platform.

Quantitative real-time PCR (qRT-PCR)

Total RNA was extracted using an RNA Extraction Kit (Accurate Biology, China) in accordance with the manufacturer's instructions. Reverse transcription used Evo M−MLV Reverse Transcription Reagents (Accurate Biology, China) by the standard protocol. SYBR Green Premix Pro Taq HS qPCR Kit (Accurate Biology, China) for quantitative PCR was performed with ABI 7500 Sequence Detection System. GADPH was used an internal reference. The level of mRNA expression was quantified using the delta-delta Ct method. All primers were purified and synthesized by Huada Company (Shenzhen, China). Primers sequences are listed in Table S1.

Flow cytometry for lymphocytes

The tumor tissue excised was minced with eye scissors and incubated in RPMI1640 medium containing DNase I (0.1 mg/ml, Roche) and Collagenase IV (0.5 mg/ml, Gibco) for 30 min at 37℃. Then, the cell suspension was filtered with a 70 μm cell strainer (Biosharp, China). The obtained cell was stained with the indicated surface antibodies for 30 min on ice, protected from light. For cytokines staining, cells were incubated with Leuko Actvtn Cktl with GolgiPlug (eBioscience, USA) for 4 h. Intracellular antibodies were added after fixation and permeabilization according to the instructions (BD Biosciences, USA). Labeled cells were analyzed on a BD LSR Fortessa using BD FACSDiva Software (BD Biosciences, USA). Compensation and analysis were performed using FlowJo v10.4.0 software. The antibodies used were purchased from BioLegend: APC anti-mouse CD3ε Antibody (Cat #: 100312); FITC anti-mouse CD8a Antibody (Cat #: 100706); PE/Cyanine7 anti-mouse IFN-γ (Cat #: 505826); PerCP/Cyanine5.5 anti-mouse Ki-67 (Cat #: 652424). The concentration of antibody was determined according to the manufacturer's instructions.

Immunofluorescence (IF)

Cells were seeded into small confocal laser dishes. AZD0156 were added into the confocal dish and then were exposed to IR. After 24 h, cells were fixed in 4 % paraformaldehyde for 30 min, permeabilized with 0.5 % Triton X-100, and blocked with goat serum. Primary antibodies were incubated overnight, and secondary antibodies were incubated at room temperature for 30 min. The primary antibodies and concentrations used are as follows: Anti-dsDNA for human (1:50, santa cruz, sc-80772), Anti-TFAM (1:200, Proteintech, 23996–1-AP), Anti-ATM (phospho S1987) (1:100, Abcam, ab315019), Anti-PD-L1/CD274 Monoclonal antibody (1:250, proteintech, 66248–1). The secondary antibodies and concentrations used are as follows: Goat anti-Mouse Alexa-488-labeled secondary antibodies (1:200, Bioss), Goat anti-Rabbit IgG (H+L) Highly Cross-Adsorbed Secondary Antibody, Alexa Fluor™ 594 (1:800, Invitrogen, A-11037). DAPI (Beyotime, C1005) was used for nuclei staining and Mito-Tracker Red CMXRos (Beyotime, C1035) was used for mitochondria staining according to the manufacturer's instructions. Confocal microscopy was performed using an Olympus FV1000 Confocal Microscope.

Construction of rho⁰ cell line

4×10^5 cells were seeded into a cell culture flask and cultured with complete growth medium until the cells adhered to the surface. The culture medium was then replaced with RPMI1640 complete medium containing 500 ng/mL ethidium bromide, 1 mM sodium pyruvate, and 50 μg/mL uridine pyrimidine, and the cells were further cultured for 10 days. The medium was refreshed and cells were passaged regularly. The successful knockout of mitochondrial DNA was confirmed by immunofluorescence.

CD8+ T cell chemotaxis assay

Naïve CD8+ T cells were isolated from the spleens of C57BL/6 mice using the EasySep™ Mouse Naïve CD8+ T Cell Isolation Kit. The isolated naïve CD8+ T cells were then activated with Mouse T Activator Dynabeads (Thermo Fisher Scientific) and recombinant Mouse IL-2 protein (R&D Systems, Catalog #: 402-ML) for 10 days. After activation, effector CD8+ T cells were collected using a magnetic plate and resuspended in RPMI1640 serum-free medium. MC38 cells were pre-seeded in 24-well plates and treated with radiation (6 Gy) or combined with AZD0156 (4 uM) and NAC (5 uM). After 8 h, the medium was replaced with fresh, drug-free medium and cells were further cultured for 24 h. The supernatant was collected and transferred to a new 24-well plate (lower chamber). A cell suspension containing 2.5×10^4 effector CD8+ T cells was placed into the upper chamber of a 5 μm Transwell insert. After 24 h of incubation, the number of cells in the lower chamber was assessed by flow cytometry.

Flow cytometry for PD-L1 expression

Cells were detached using trypsin without EDTA and washed three times with PBS. Cells were resuspended in 200 ul PBS, incubated with the PD-L1 antibody on ice in the dark for 30 min, and then washed once with PBS. Finally, cells were resuspended in 200 ul PBS for flow cytometry analysis. Antibodies used: PE/Cyanine7 anti-mouse CD274 (B7-H1, PD-L1) Antibody (1:100) and PE anti-human CD274 (B7-H1, PD-L1) Antibody (1:100).

Chromatin immunoprecipitation (ChIP)

ChIP assays were performed using Chromatin Immunoprecipitation kit (Chromatin, USA). Immunoprecipitation reactions were
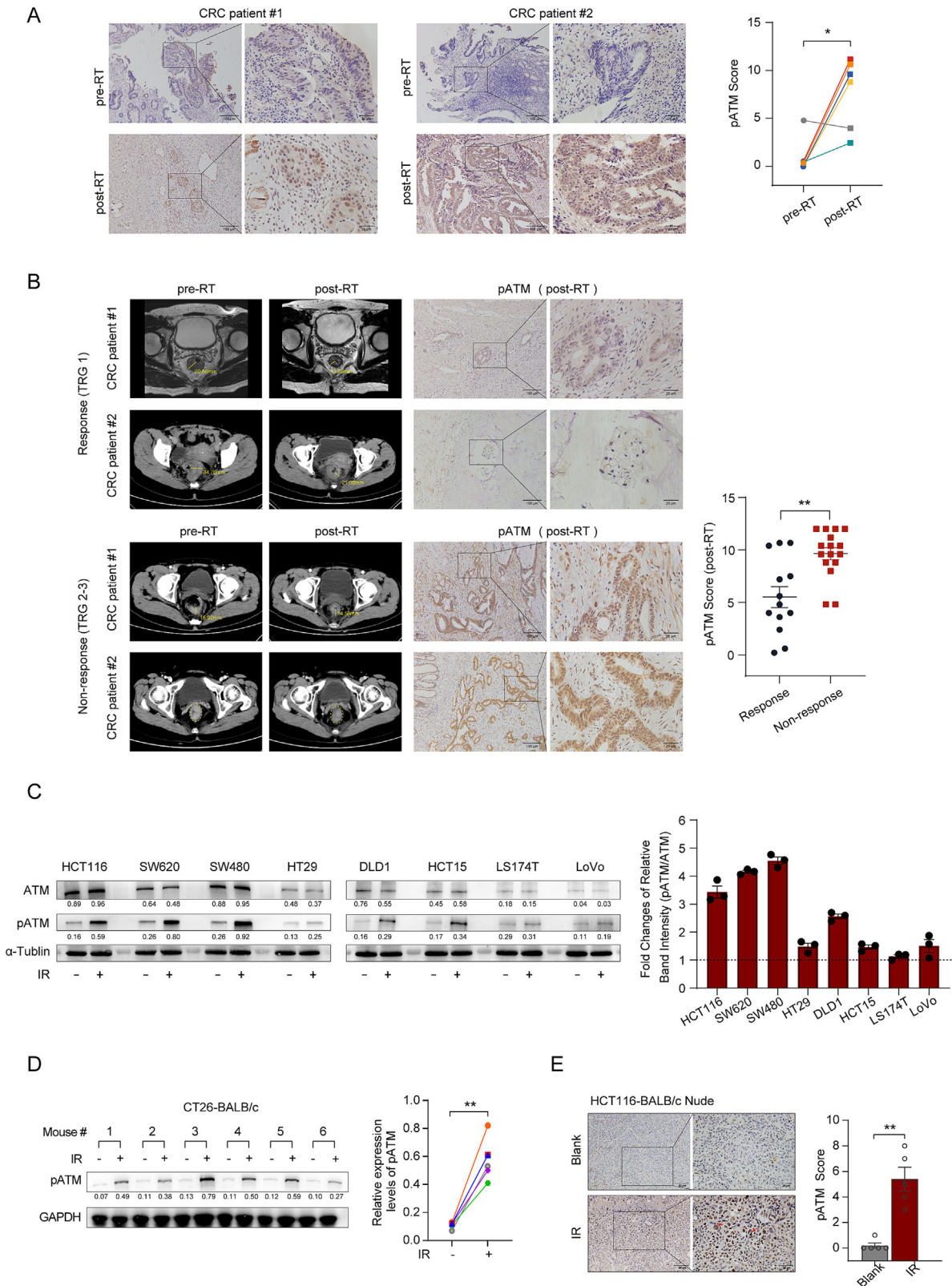
Fig. 1. ATM emerges as a promising target for enhancing the efficacy of radiotherapy in colorectal cancer. **A.** Representative images of phosphorylated ATM (pATM) IHC staining of matched rectal tumor samples from the same patients before and after RT. **B.** Representative images of pATM IHC staining of rectal tumor surgical specimens post-RT. Patients were classified into either responders (TRG = 1) or non-responders (TRG = 2–3). Matched radiographic images from corresponding patients before and after RT are displayed. **C.** Western blot analysis was conducted to evaluate the ratio of pATM to ATM before and after irradiation (IR, 8 h after 6 Gy). The statistical graph illustrates the fold change in the ratio, calculated as: (pATM/ATM ratio post-IR − pATM/ATM ratio pre-IR) / pATM/ATM ratio pre-IR. **D.** Phospho-ATM expression of the CT26 tumors was assessed by western blot. Paired samples were derived from CT26 tumors grown in BALB/c mice, with one tumor subjected to IR (8 Gy × 2) and the other remaining non-IR. Tumors were harvested on day 14 after IR treatment. **E.** Phospho-ATM expression of HCT116 tumors was evaluated by IHC. Samples were from HCT116 tumors grown in BALB/c-nu/nu mice with or without IR (5 Gy × 2) (n = 5). Tumors were harvested on day 12 after IR treatment. Data are represented as mean ± SEM of at least three replicates. *p < 0.05, **p < 0.01, ***p < 0.001, ****p < 0.0001.

Y. Xie, Y. Liu, M. Lin et al.
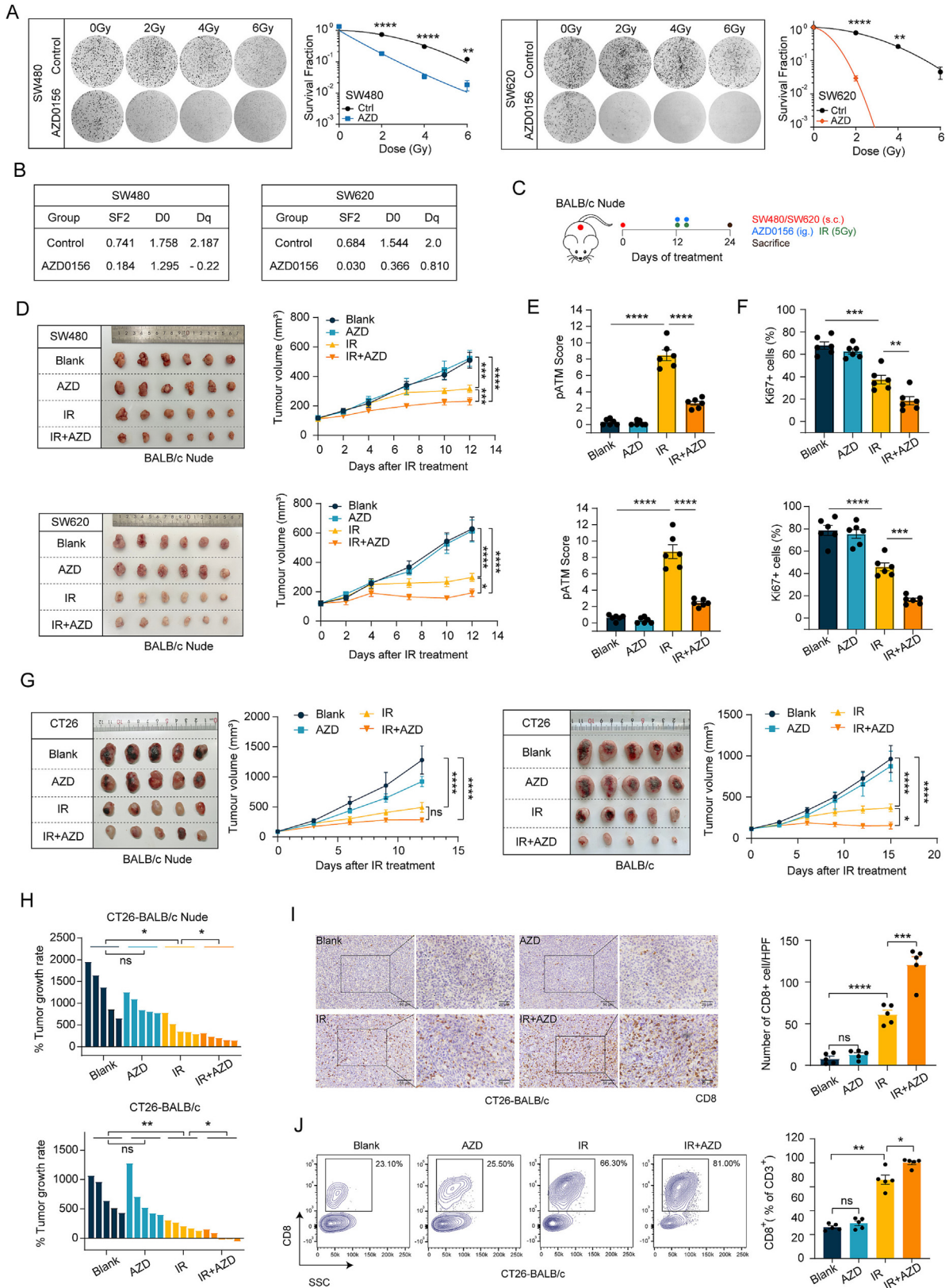
performed with 5 ug antibody against p65 (ABclonal, A19653) or with IgG, used as a negative control. Purified DNA was suspended subsequently for following qRT-PCR analysis. Primer sequences are listed in Table S1.

Co-immunoprecipitation (Co-IP)

Total proteins were extracted using cell lysis buffer containing protease and phosphatase inhibitors. The lysate (100 ug of protein) was incubated with the corresponding antibodies overnight at 4℃. The protein-antibody complexes were then incubated with protein A/G magnetic beads for 5 h at 4℃. Immunoprecipitation was collected by centrifugation, and the bead complexes were washed four times with PBS. After the final wash, the protein A/G magnetic beads were eluted by boiling in $5 \times$ SDS sample buffer, and the proteins were analyzed by Western blot. Antibody: ATM Antibody (G-12): (1:500, Santa Cruz, sc-377293), NEMO Antibody (1:500, ABclonal, A12536), ATM phospho Ser1981 antibody (1:1000, proteintech, 39529).

Enzyme-linked immunosorbent assay (ELISA)

To detect biochemical indicators in mice, blood was collected from the inner canthus at three time points: before IR, during IR, and after IR. The collected whole blood was left at room temperature for 2 h, followed by centrifugation to obtain serum. The ELISA kits used included the Mouse Aspartate Aminotransferase (AST) ELISA Kit, Mouse Alanine Aminotransferase (ALT/GPT) ELISA Kit (CUSABIO, China), Mouse Troponin T (TnT) ELISA Kit (MEIMIAN, MM-44145H1), and Mouse Creatine Kinase Isoenzyme MB (CK-MB) ELISA Kit (MEIMIAN, MM-43703H1). For cell experiments, supernatants from different treatment conditions were collected for ELISA. The ELISA kits used included the Human Interferon β1 (IFN-β1) ELISA Kit (MEIMIAN, MM-51652H1), Human CXC Chemokine Ligand 10 (CXCL10) ELISA Kit (MEIMIAN, MM-2166H1), and Human CXC Chemokine Ligand 11 (CXCL11) ELISA Kit (MEIMIAN, MM-60846H1).

Patient samples

The paraffin sections from pre-radiotherapy of biopsy and post-radiotherapy surgical specimens in 29 CRC patients were retrospectively retrieved from the Nanfang Hospital of Southern Medical University. These patients have locally advanced rectal cancer, classified as stage III or stage II with high-risk factors (EMVI+/CRM+/low-lying rectal cancer). They receive standard neoadjuvant chemoradiotherapy with a radiation dose of 50 Gy/25F, combined with capecitabine during radiation. After radiotherapy, they undergo 4–6 cycles of FOLFOX or CAPEOX chemotherapy, followed by total mesorectal excision (TME) 2–4 weeks later. During radiation, capecitabine monotherapy is used as concurrent chemotherapy. After radiation, the patient receives 4–6 cycles of FOLFOX or CAPOX chemotherapy, followed by total mesorectal excision (TME) 2–4 weeks later. We guaranteed that the patient data would be used only for this study and not for any other purposes, and adhered to the Declaration of Helsinki.

Ethics statement

All experiments involving animals were conducted according to the ethical policies and procedures approved by the Animal Ethics Committee of Guangdong Medical Laboratory Animal Center (Approval no. C202304-4).

The paraffin sections from patients used were approved by the Ethics Committee of Nanfang Hospital of Southern Medical University (Approval no. NEFC-2022–367).

Statistical analysis

SPSS 21 and GraphPad prism 9.0 software were used for statistical analysis. For comparison between the two groups, Student's *t*-test or Mann-Whitney *U* test was applied on parametric and non-parametric datasets respectively. For comparisons of three or more groups, data were analyzed by one-way ANOVA or two-way ANOVA. Data are expressed as means ± SEM. Significant differences are indicated by *ns., no significant differences, $^*p < 0.05$, $^{**}p < 0.01$, $^{***}p < 0.001$, and $^{****}p < 0.0001$.

Results

ATM emerges as a promising target for enhancing the efficacy of radiotherapy in colorectal cancer

In response to radiation-induced DNA damage, ATM rapidly autophosphorylates at serine 1981, playing a key role in the DNA damage response [11]. We assessed ATM activation post-radiotherapy by performing immunohistochemical (IHC) staining for phosphorylated ATM (pATM) in paired tumor samples from six rectal cancer patients. We observed a notable increase in pATM levels post-radiotherapy, indicating ATM activation (Fig. 1A). Subsequently, we analyzed the relationship between pATM levels in CRC samples after radiotherapy and tumor radiotherapy response. Tumor regression grade (TRG) assesses the pathological response of tumors to radiotherapy after neoadjuvant chemoradiotherapy. We classified 29 patients into a "Response group" (TRG = 1, n = 13) and a "Non-response group" (TRG = 2–3, n = 16). IHC revealed lower pATM levels in patients with favorable radiotherapy responses and higher levels in poor responders (Fig. 1B). Next, we investigated the radiosensitization potential of ATM in CRC through comprehensive in vitro and in vivo experiments. We treated eight different CRC cell lines with irradiation (IR) and assessed

Fig. 2. Targeted inhibition of ATM enhances the radiation sensitivity and post-radiation antitumor immunity of colorectal cancer. **A.** A colony formation assay was conducted to evaluate the radiosensitizing effect of AZD0156 (100 nM) exposure for 24 h under increasing doses of IR. Survival fractions were analyzed using the linear-quadratic (L-Q) model. **B.** Radiobiological parameters reflected the radiosensitization efficacy were calculated by using multi-target single-hit model. **C.** Schematic representation of SW480 and SW620 xenografts (s.c.) in BALB/c-nu/nu (nude) mice treated with blank control, AZD0156 (10 mg/kg), IR (5 Gy × 2), or IR combined with AZD0156. **D.** Tumor images and growth curves are presented, with the upper section showing the SW480 subcutaneous tumor model and the lower section showing the SW620 subcutaneous tumor model. **E.** The inhibitory effect of AZD0156 was evaluated using pATM IHC, with the staining scores for pATM presented in the figure. **F.** Tumor proliferation was evaluated using Ki67 IHC, and the percentage of Ki67-positive cells is shown in the figure. The upper section corresponds to the SW480 tumor model, while the lower section corresponds to the SW620 tumor model. **G.** Tumor images and growth curves are shown for CT26 subcutaneous tumor models in BALB/c nude mice (left panel) and BALB/c mice (right panel). Mice were treated with blank control, AZD0156 (10 mg/kg), IR (8 Gy × 2), or IR combined with AZD0156. **H.** Tumor growth rates are shown for subcutaneous tumor models in BALB/c nude mice (upper panel) and BALB/c mice (lower panel). **I.** IHC staining of CD8 + lymphocytes in CT26 tumors of BALB/c mice. **J.** Flow cytometry was used to analyze CD8+ T cell infiltration in CT26 tumors. Data are represented as mean ± SEM of at least three replicates. $^*p < 0.05$, $^{**}p < 0.01$, $^{***}p < 0.001$, $^{****}p < 0.0001$.
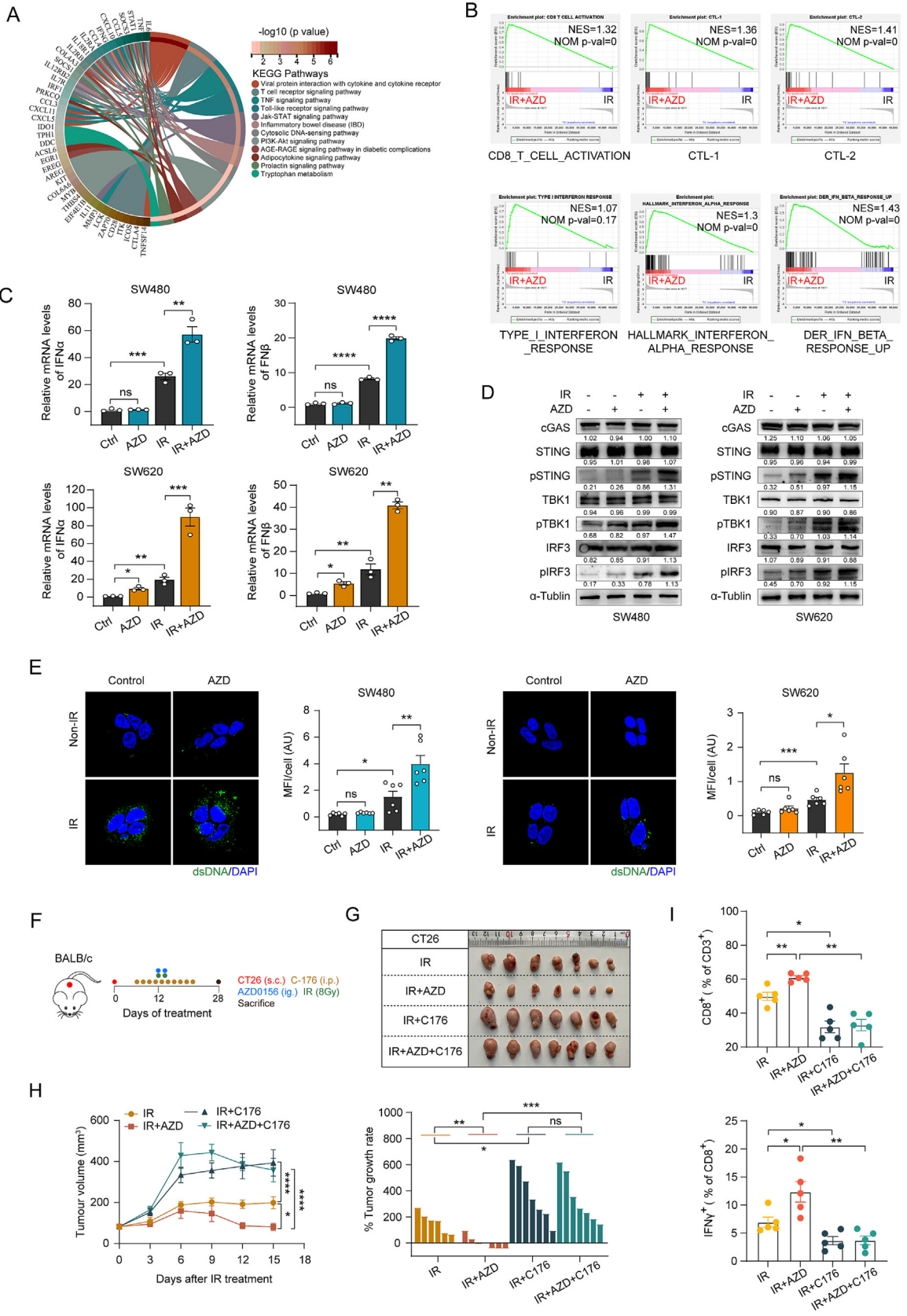
total ATM and phosphorylated ATM levels pre- and post-IR. Results demonstrated that in most CRC cell lines, the level of pATM increases after irradiation, while the total ATM level remains largely unchanged. The pATM/ATM ratio significantly increased in most CRC cell lines post-IR (Fig. 1C). Analysis of several GSE datasets also indicated no significant change in ATM transcription levels in colorectal cancer cells or tissues pre- and post-radiation (Supplementary Fig. 1B). Further, SW620 cells were treated with different doses of radiation, and ATM phosphorylation levels were measured at different time points after 6 Gy of radiation. Radiation significantly induced ATM phosphorylation, which increased with dose and time (Supplementary Fig. 1A). Additionally, paired CT26 subcutaneous tumor samples revealed higher pATM protein levels in irradiated tumors compared to non-irradiated controls (Fig. 1D). IHC staining of HCT116 subcutaneous tumors also showed increased pATM levels following localized radiation (Fig. 1E). Collectively, our data confirm significant ATM activation by radiation in CRC cells, supporting its potential as a radiosensitization target.

Targeted inhibition of ATM enhances the radiation sensitivity and post-radiation antitumor immunity of colorectal cancer

First, we selected the cell lines SW620 and SW480, which exhibited a greater relative difference in the pATM/ATM ratio before and after IR (Fig. 1C), for subsequent experiments. We used lentivirus to silence ATM expression in these cells, selecting the most efficient constructs, shATM #2 and shATM #3, for further experiments (Supplementary Fig. 2A). EdU assays showed that before radiation, ATM knockdown had little effect on SW620 and SW480 cell proliferation. However, after radiation, proliferation significantly decreased in shATM cells compared to shNC controls (Supplementary Fig. 2B). Similar trends were observed in the clonogenic assay and the CCK8 assay (Supplementary Fig. 2C, 2E). To quantify this effect, we applied the linear-quadratic model to analyze survival fractions, generating survival curves that further confirmed increased sensitivity in shATM cells (Supplementary Fig. 2C, right panel). Radiobiological parameters such as SF2 (the survival fraction at 2 Gy), D0 (the dose reducing the survival rate by 37 %), and Dq (the capacity of cells to repair sublethal damage) were calculated using the multi-target single-hit model. Results showed that these parameters were lower in ATM-knockdown cells compared to controls (Supplementary Fig. 2D), suggesting that downregulation of ATM significantly enhances radiation sensitivity in CRC cells.

AZD0156, a selective oral ATM inhibitor, boasts favorable preclinical pharmacokinetics and a clinically acceptable effective dose [5]. The impact of AZD0156 on radiation sensitivity in colorectal cancer, as well as the potential synergistic effects of combined radiotherapy, warrant further exploration. Western blot analysis confirmed that AZD0156 effectively inhibited ATM phosphorylation and downstream CHK2 activation following IR (Supplementary Fig. 2F). We employed the EdU assay to evaluate the effect of AZD0156 on cellular radiation sensitivity. The results revealed that while AZD0156 alone had minimal impact on cell proliferation in the absence of irradiation, its combination with radiation significantly reduced cell proliferation (Supplementary Fig. 2G). This radiation sensitization effect was further confirmed by clonogenic assays (Fig. 2A), with SF2, D0, and Dq values in ATM inhibitor-treated cells lower compared to the control group, indicating increased radiation sensitivity (Fig. 2B). Additionally, Radiosensitization increased with higher AZD0156 concentrations in CT26 and MC38 murine CRC cell lines (Supplementary Fig. 2H), a finding further supported by similar results from the CCK8 assay (Supplementary Fig. 2I).

Research suggests that the effectiveness of ATM inhibitors in enhancing radiosensitivity may be influenced by TP53 status [12]. However, this relationship remains unclear in CRC cells. To investigate, we assessed the response of various CRC cell lines to AZD0156. Both clonogenic survival and cytotoxicity assays indicated that TP53 wild-type LoVo cells, as well as TP53-mutant SW480 and Caco2 cells, showed a stronger radiosensitizing response to ATM inhibition. In contrast, TP53-mutant HT29 and HCT15 cells, along with TP53 wild-type HCT116 cells, exhibited relatively weaker responses (Supplementary Fig. 2J, 2 K). Overall, these findings demonstrate that ATM inhibitors significantly enhance radiosensitivity in CRC cells, and this effect appears to be independent of TP53 status.

Based on in vitro cellular assays, we further validated the effect of AZD0156 on the radiosensitivity of tumors in vivo. Human CRC cells SW480 and SW620 were implanted subcutaneously into nude mice to establish xenograft models. When the tumor volume reached 100–150 mm^3, the mice were divided into four groups: (i) a blank control group treated with PBS; (ii) a monotherapy group treated with AZD0156 alone (AZD); (iii) a radiation therapy alone group (IR); and (iv) a combination therapy group (IR + AZD) (Fig. 2C). IHC staining of tumor tissues revealed that radiotherapy significantly induced ATM phosphorylation levels compared to the control group, while AZD0156 treatment notably inhibited radiation-induced ATM phosphorylation (Fig. 2E and Supplementary Fig. 3A). AZD0156 monotherapy had little effect on SW480 and SW620 tumor growth. However, radiation therapy significantly slowed tumor growth, and the combination therapy further enhanced this effect (Fig. 2D). IHC results also indicated that the combination therapy minimized the proportion of Ki-67 positive cells within the tumors (Fig. 2F and Supplementary Fig. 3A).

Subsequently, subcutaneous xenograft experiments with murine CRC cells MC38 in immunocompetent C57BL/6J mice indicated that the combined therapy significantly inhibited tumor growth, clearly superior to the PBS control, individual drug treatment, and radiation therapy alone groups (Supplementary Fig. 3B, 3C). Tumor regression occurred only in the combined therapy group (Supplementary Fig. 3D). Both the radiation and combined therapy

Fig. 3. Targeting ATM could activate the STING pathway by increasing cytoplasmic DNA levels following radiation exposure. **A.** RNA-seq gene set enrichment analysis of CT26 tumors treated with IR (8 Gy × 2) or IR combined with AZD0156 (10 mg/kg). **B.** CD8 T cell activation-related pathways and IFN-related pathways were enriched in the IR plus AZD0156 group compared to the IR-alone group. **C.** Expression levels of IFNβ and IFNα in SW620 and SW480 cells treated with control, AZD0156 (2 uM), IR (6 Gy), or the combination of IR and AZD0156, analyzed by qRT-PCR. **D.** Protein expression of STING signaling in SW480 and SW620 cells treated with control, AZD0156, IR, or the combination of IR and AZD0156. Total and phosphorylated levels of STING, TBK1, and IRF3 were assessed by western blot after 48 h. **E.** SW480 and SW620 CRC cells with control, AZD0156 (2 uM), IR (6 Gy) or combination treatment were stained with anti-dsDNA (green) antibody and DAPI. **F.** Effect of STING inhibition on radiation responsiveness in subcutaneous CT26 tumors implanted in BALB/c mice. Mice were treated with IR (8 Gy × 2), IR with AZD0156 (10 mg/kg), IR with C-176 (5 mg/kg), or IR with both AZD0156 and C-176. **G.** Tumor images from the four treatment groups were captured on the day of harvest. **H.** Tumor growth curves (left panel) and individual tumor growth rates (right panel) for each mouse are shown. **I.** Flow cytometry analysis of CT26 tumors in BALB/c mice. The percentages of CD8+ T cells and activated IFNγ + CD8+ T cells were analyzed on day 14 post-IR treatment. Data are represented as mean ± SEM. *p < 0.05, **p < 0.01, ***p < 0.001, ****p < 0.0001. (For interpretation of the references to colour in this figure legend, the reader is referred to the web version of this article.)

Mito-Tracker Red CMXRos TFAM DAPI
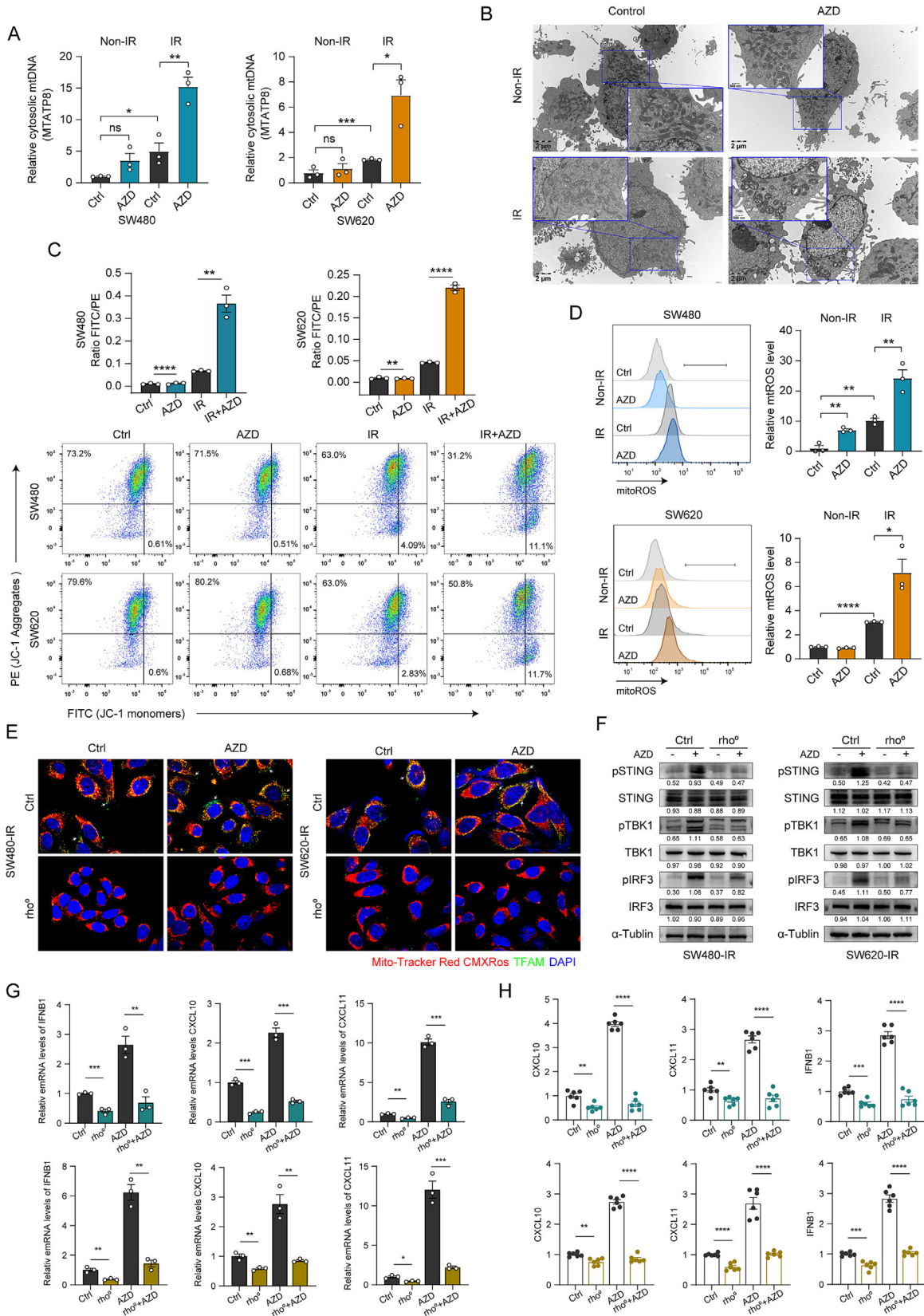
groups had significantly longer survival than the control group, with no deaths during the observation period (Supplementary Fig. 3E).

Ionizing radiation activates the tumor immune microenvironment, promoting anti-tumor responses [13,14]. We studied the effect of ATM inhibitors on tumor immune status during radiotherapy by implanting CT26 cells into T cell-deficient nude mice and immunocompetent BALB/c mice. AZD0156 improved radiotherapy response in both, with stronger tumor suppression in BALB/c mice (Fig. 2G). In BALB/c mice, combination therapy outperformed radiotherapy alone, leading to tumor regression (Fig. 2H).

Radiotherapy can increase the infiltration of CD8+ T cells in the tumor microenvironment [15], but the impact of combined ATM inhibitors on CD8+ T cells within the colorectal cancer microenvironment remains unclear. CD8 IHC staining of CT26 tumor tissues showed that AZD0156 alone had no effect on CD8+ T cell infiltration, while radiotherapy increased it. Combination therapy further enhanced CD8+ T cell infiltration (Fig. 2I). Flow cytometry showed that radiotherapy significantly boosted CD8+ T cell proportions compared to controls and monotherapy, with combination therapy enhancing this effect (Fig. 2J). Neither radiotherapy nor AZD0156 altered Ki67 + CD8+ T cell proportions (Supplementary Fig. 3G).

In summary, targeting ATM increases the radiosensitivity of colorectal cancer cells both in vitro and in vivo. The ATM inhibitor AZD0156 may also boost antitumor immune responses by enhancing CD8+ T cell infiltration, further improving radiosensitivity. These findings highlight ATM as a promising target for radiosensitization in colorectal cancer therapy.

Targeting ATM could activate the STING pathway by increasing cytoplasmic DNA levels following radiation exposure

To investigate how ATM inhibition boosts post-radiation antitumor immunity, we conducted transcriptomic sequencing (RNA-seq) on tumors from mice treated with radiation alone or in combination with AZD0156. Gene Set Enrichment Analysis (GSEA) of the RNA-seq data identified enriched pathways in the combination therapy group. The Cytosolic DNA-sensing pathway attracted our attention (Fig. 3A) because the cGAS-STING signaling pathway plays an important role in mediating radiation-induced antitumor effects [16]. Cyclic GMP-AMP synthase (cGAS), a cytosolic DNA sensor, detects double-stranded DNA, activating the Stimulator of interferon genes (STING) pathway and boosting transcription of type I interferon genes, crucial for antitumor immunity [17]. GSEA results also unveiled enrichment in pathways associated with CD8 T-cell activation, CTL-1, CTL-2 pathways, and multiple interferon-related pathways in the combination therapy group, indicating activation of immune-related pathways and enhanced type I interferon response (Fig. 3B). qRT-PCR validation in vitro and in vivo confirmed increased expression of interferon genes with combination therapy (Fig. 3C and Supplementary Fig. 4A). Western blot analysis showed that IR activated the STING pathway, indicated

by increased levels of Phospho-STING (pSTING), Phospho-TBK1 (pTBK1), and Phospho-IRF3 (pIRF3). Combination therapy further enhanced this activation (Fig. 3D). Western blot analysis of MC38 subcutaneous tumors confirmed significantly stronger STING signaling activation in the combination therapy group compared to the radiation-only group (Supplementary Fig. 4B). We then assessed cytoplasmic double-stranded DNA (dsDNA) levels after radiation and ATM inhibition. Immunofluorescence showed that radiation increased cytoplasmic dsDNA, and this effect was further enhanced by combination therapy (Fig. 3E). Subsequent in vivo experiments using the STING inhibitor C-176 supported these findings. CT26 cells were implanted subcutaneously in BALB/c mice, which were then divided into four groups: (i) Radiation alone (IR), (ii) AZD0156 combined with radiation (IR + AZD), (iii) C-176 combined with radiation (IR + C176), and (iv) C-176 and AZD0156 combined with radiation (IR + AZD + C176) (Fig. 3F). Combination therapy significantly inhibited tumor growth, which was reversed by STING inhibition (Fig. 3G, 3H). Western blot results confirmed that C-176 treatment significantly inhibited downstream STING signaling molecules pTBK1, pIRF3, and pSTAT1 (Supplementary Fig. 4C). Flow cytometry analyses revealed a reduction in CD8+ T cells and decreased CD8+ T cell activation following STING inhibition, indicating suppressed antitumor immunity (Fig. 3I and Supplementary Fig. 4F). Radiation can induce the release of various cytokines and chemokines, recruiting CD8+ T cells into the tumor microenvironment and enhancing antitumor immunity. RNA-seq data and qRT-PCR validation highlighted increased expression of T-cell chemokines CXCL10 and CXCL11 with combination therapy, further supporting enhanced antitumor immunity (Supplementary Fig. 4D, 4E).

In summary, inhibiting ATM may enhance STING signaling activation by increasing cytoplasmic DNA, which promotes the expression of downstream chemokines CXCL10/CXCL11, thereby increasing CD8+ T cell infiltration in the tumor microenvironment.

Targeting ATM promotes mitochondrial damage post-irradiation to facilitate STING pathway activation

Cytoplasmic DNA arises from genomic (gDNA) and mitochondrial (mtDNA) sources. ATM is a key protein involved in the repair of genomic DNA damage. Therefore, we hypothesize that inhibiting ATM may lead to the release of damaged DNA fragments into the cytoplasm by disrupting the timely repair of double-stranded genomic DNA. To evaluate cytoplasmic gDNA content, we used qRT-PCR to assess the relative abundance of the GAPDH gene encoded by the genome. Results showed that radiation increased cytoplasmic gDNA levels in SW480 and SW620 cells, but there was no significant difference compared to the combination with AZD0156 (Supplementary Fig. 5A). Recent studies have found that mtDNA also plays a role in enhancing radiation-induced immunity [10,18]. By measuring the relative abundance of the mitochondrially encoded MTATP8 gene in the cytoplasm, we found that radia-

Fig. 4. Targeting ATM promotes mitochondrial damage post-irradiation to facilitate STING pathway activation. **A.** The cytosolic abundance of the MTATP8 DNA sequence was measured by qPCR 24 h post-IR. **B.** Mitochondrial morphological changes were examined using transmission electron microscopy in SW620 cells collected 24 h post-IR. **C.** Flow cytometric analysis detected changes in mitochondrial membrane potential, with a reduced green/red fluorescence intensity ratio (FITC/PE) indicating mitochondrial depolarization. Samples were collected 24 h after treatment with IR (6 Gy), AZD0156 (2 uM), or their combination. **D.** Mitochondrial ROS levels were examined by flow cytometric detection 24 h post-IR. **E.** Control and rho⁰ cells (mtDNA-depleted) were treated with IR (6 Gy) alone or combined with AZD0156 (2 uM). Cells were co-stained with MitoTracker Red CMXRos (mitochondria, red), anti-TFAM (green), and DAPI. **F.** Western blot analysis of STING signaling protein expression in SW480 and SW620 control and rho⁰ cells treated with IR alone or in combination with AZD0156. Total and phosphorylated levels of STING, TBK1, and IRF3 were evaluated 48 h post-treatment. **G.** qRT-PCR analysis of IFNB1, CXCL10, and CXCL11 expression in control and rho⁰ cells treated with IR alone (6 Gy) or in combination with AZD0156 (2 uM), 24 h post-IR. **H.** ELISA analysis of IFNB1, CXCL10, and CXCL11 levels in cell supernatants from control and rho⁰ cells treated with radiation alone or in combination with AZD0156. Data are represented as mean ± SEM. *p < 0.05, **p < 0.01, ***p < 0.001, ****p < 0.0001. (For interpretation of the references to colour in this figure legend, the reader is referred to the web version of this article.)

Y. Xie, Y. Liu, M. Lin et al.
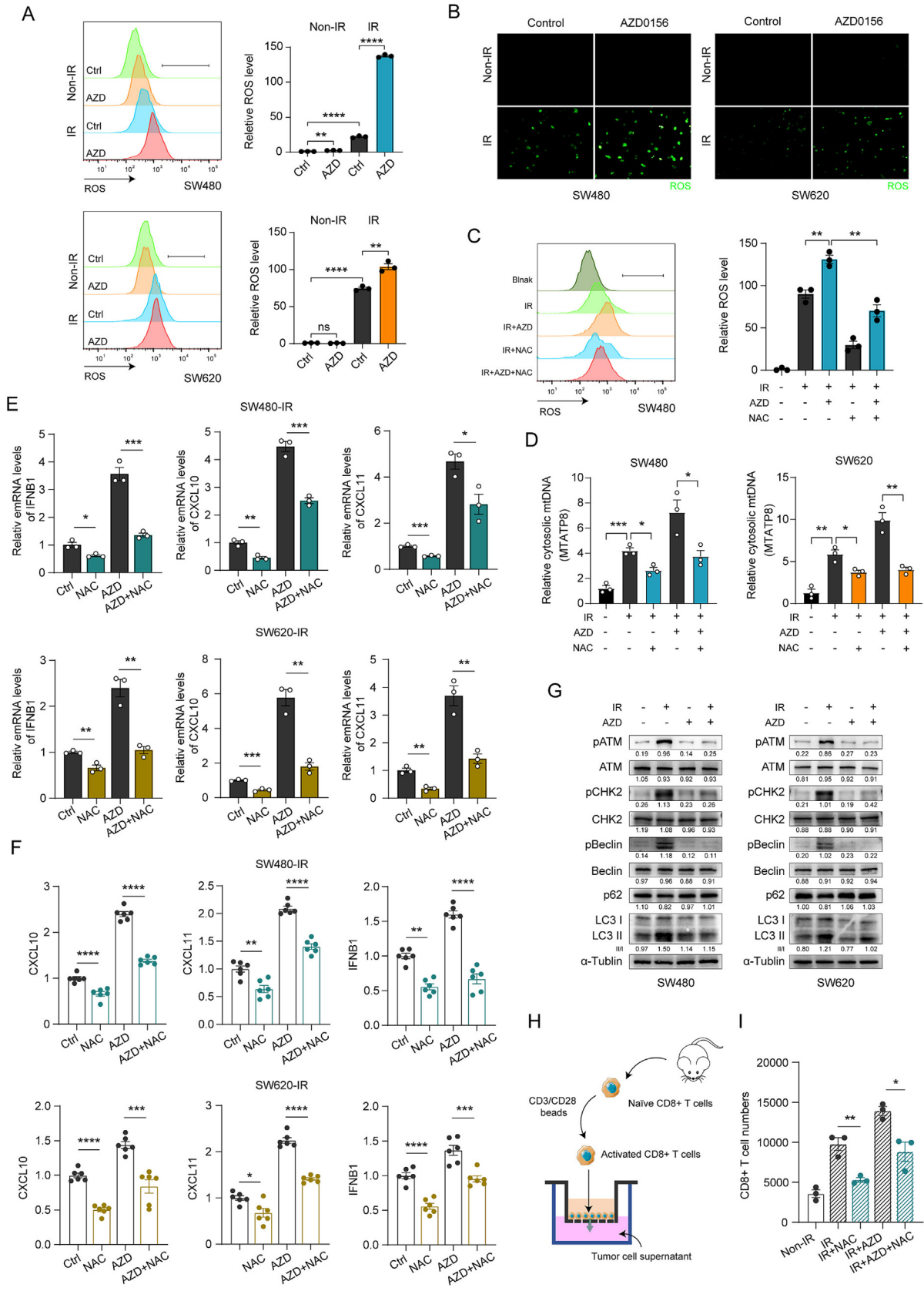
tion increased mtDNA content in the cytoplasm of SW480 and SW620 cells. This increase was further enhanced by the combination with an ATM inhibitor (Fig. 4A). Damaged mitochondria exhibit increased membrane permeability, which may facilitate the release of mtDNA into the cytoplasm. Transmission electron microscopy showed post-radiation mitochondrial damage, characterized by enlarged and swollen morphology. The combination of ATM inhibition and radiation caused more severe mitochondrial damage, including disruption, breakage, or loss of mitochondrial cristae, along with significant vacuolar degeneration (Fig. 4B). Correspondingly, more apoptosis was observed in the combination treatment group than in the radiation-only group (Supplementary Fig. 5B). Changes in membrane potential are a hallmark of mitochondrial damage, prompting us to conduct JC-1 (membrane potential indicator) staining. Compared to mitochondria with high membrane potential, which display red fluorescence, damaged mitochondria show brighter green fluorescence signals. Flow cytometry analysis revealed that radiation increased the green/red fluorescence ratio, and this ratio was further significantly enhanced following combination treatment with AZD0156 (Fig. 4C). Ionizing radiation generates ROS by damaging mitochondria, causing oxidative stress and indirectly damaging DNA [6]. Flow cytometry measuring post-radiation mitochondrial ROS (mitoROS) levels found that radiation combined with an ATM inhibitor further increased radiation-induced mitoROS (Fig. 4D). To determine whether the accumulation of mtDNA is essential for the enhanced type I interferon (IFN) response induced by ATM inhibition after radiation, we cultured cells in low concentrations of ethidium bromide (EthBr) to deplete their mtDNA, creating mtDNA-depleted cells (rho^0 cells). IF analysis showed that ATM inhibition enhanced radiation-induced accumulation of cytoplasmic mitochondria (increased TFAM staining, green fluorescence). In contrast, green fluorescence was nearly absent in rho^0 cells, indicating depletion of mtDNA (Fig. 4E). Furthermore, mtDNA depletion abolished the activation of the STING-type I IFN signaling pathway triggered by radiation combined with AZD0156 (Fig. 4F) and decreased the expression levels of IFNB1, CXCL10, and CXCL11 (Fig. 4G). ELISA results further confirmed a reduction in the release of these cytokines (Fig. 4H).

Reducing ROS accumulation after radiation attenuates immune activation induced by ATM inhibition

Damaged mitochondria not only leads to cell apoptosis but also generates increased levels of ROS, further damaging the mitochondrial membrane [19,20]. Therefore, we investigated whether the accumulation of ROS is a key factor in enhancing the type I IFN response induced by targeting ATM after radiation. We used the DCFH-DA-FITC probe to label ROS and assess the impact of ATM inhibition on intracellular ROS levels. The combination of AZD0156 with radiation further increased the accumulation of intracellular ROS compared to the radiation-only group (Fig. 5A, 5B). We hypothesize that ATM inhibitors may promote mitochondrial damage by upregulating radiation-induced ROS, thereby triggering cell apoptosis and the leakage of mitochondrial DNA. Subsequently, we pre-treated cells with the ROS scavenger NAC before radiation, and flow cytometry results showed that NAC partially removed ROS induced by radiation alone and in combination with AZD0156 (Fig. 5C). qRT-PCR results suggested that NAC pre-treatment reduced the upregulation of MTATP8 DNA content in the cytoplasm induced by radiation and combined treatments (Fig. 5D), and the apoptosis of cells post-radiation also decreased (Supplementary Fig. 5B). Additionally, the removal of ROS reduced the increased expression of IFNB1, CXCL10, and CXCL11 in response to radiation combined with AZD0156 (Fig. 5E), and ELISA results further indicated a decrease in the release of these cytokines (Fig. 5F). Recent studies have shown that stress-induced ATM-CHK2-Beclin1 signaling pathway triggers autophagy, which can eliminate damaged mitochondria under oxidative stress, thereby maintaining cellular ROS homeostasis [21]. We have previously confirmed the activation of the ATM/CHK2 signaling pathway after radiation (Supplementary Fig. 2F). Additionally, transmission electron microscopy revealed an increase in autophagosomes in SW620 cells after radiation (Supplementary Fig. 5C). Radiation treatment induced cellular autophagy, as evidenced by the decrease in the autophagy substrate p62 and the conversion of the non-lipidated form of LC3 (LC3-I) to its phosphatidylethanolamine-conjugated form (LC3-II). Inhibition of ATM suppresses the activation of CHK2/Beclin1 and the subsequent cellular autophagy (Fig. 5G). This may represent one of the potential mechanisms leading to the accumulation of ROS and damaged mitochondria.

To further explore the impact of ROS accumulation on immune activation, we performed an in vitro CD8+ T cell chemotaxis assay. Naïve CD8+ T cells were purified from mouse spleens and activated using T-activator CD3/CD28 beads and IL-2. MC38 cells were treated with radiation or drug combinations for 8 h, then cultured without drugs for 1 day before collecting the supernatant. Activated CD8+ T cells were placed in the upper chamber, and MC38 cell supernatant was added to the lower chamber to allow T cell migration for 24 h (Fig. 5H). The lower chamber medium was subsequently collected, and the number of cells was assessed by flow cytometry. The results indicated that, compared to the IR-alone group, the use of the ATM inhibitor significantly enhanced CD8+ T cell migration. However, ROS scavenging using NAC significantly reduced CD8+ T cell chemotaxis (Fig. 5I).

In summary, ATM inhibition enhances the accumulation of mitochondrial ROS and mitochondrial damage induced by radiation. This process not only increases cell apoptosis but also promotes the release of mitochondrial DNA into the cytoplasm, activating the STING-type I IFN signaling pathway and facilitating the recruitment of CD8+ T cells.

Fig. 5. Reducing ROS accumulation after radiation attenuates immune activation induced by ATM inhibition. **A.** Flow cytometry analysis of ROS generation in DCFH-DA-stained SW480 and SW620 cells treated with IR (6 Gy), AZD0156 (2uM), or their combination. **B.** Fluorescent imaging of SW480 and SW620 cells demonstrating the effect of AZD0156 on intracellular ROS production following IR (6 Gy). ROS is shown as green fluorescence. **C.** The ROS scavenger NAC (5 mM) was used to reduce IR-induced or IR plus AZD-induced ROS levels in SW480 cells. **D.** The abundance of the cytoplasmic MTATP8 DNA sequence after NAC treatment was analyzed by qRT-PCR. **E.** Cells were treated with IR alone or IR combined with AZD0156, with or without the addition of NAC. Expression levels of IFNB1, CXCL10 and CXCL11 were analyzed by qRT-PCR 24 h post-IR. **F.** ELISA quantified CXCL10, CXCL11 and IFNB1 levels in cell supernatants from the four treatment groups. **G.** Western blot analysis was used to assess protein expression in the ATM/CHK2/Beclin signaling pathway in SW480 and SW620 cells treated with control, IR (6 Gy), AZD0156 (4uM), or their combination.Total and phosphorylated levels of ATM, CHK2, Beclin1, and autophagy-related proteins p62 and LC3 were assessed by western blot after 48 h. **H.** Schematic diagram of ex vivo chemotaxis assay of CD8+ T cell activation and migration. **I.** Flow cytometry was used to quantify the number of CD8+ T cells that migrated to the lower chamber. The supernatants were derived from tumor cells treated with Non-IR, IR alone, IR combined with NAC, IR combined with AZD0156, or a combination of all three treatments. Data are represented as mean ± SEM. *p < 0.05, **p < 0.01, ***p < 0.001, ****p < 0.0001. (For interpretation of the references to colour in this figure legend, the reader is referred to the web version of this article.)
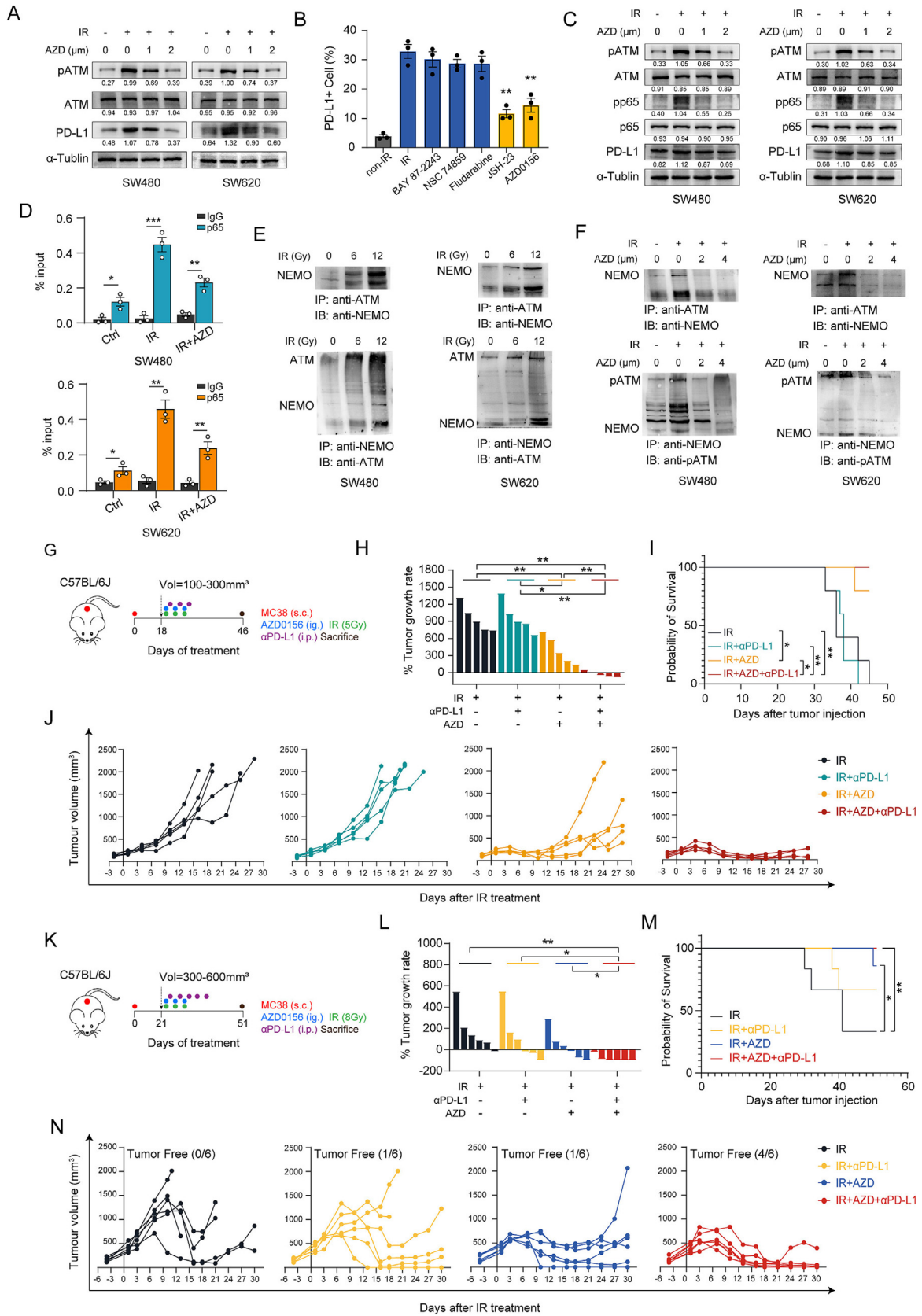
Triple therapy combining radiotherapy, AZD0156, and anti-PD-L1 blockade significantly enhances antitumor activity

While radiotherapy combined with immune checkpoint inhibitors (ICIs) has synergistic effects, its efficacy in neoadjuvant rectal cancer treatment remains to be improved [22]. Consequently, optimizing this treatment approach has become a key focus of clinical research. In this study, we utilize animal models to evaluate whether the combination of AZD0156 with radiotherapy and ICIs can effectively enhance antitumor efficacy. A key challenge in antitumor immune activation is the radiation-induced upregulation of PD-L1 on tumors [14,15]. We observed that radiation alone increased PD-L1 expression on CT26 and MC38 cells. When combined with AZD0156, PD-L1 expression decreased slightly, but remained higher than in the control and monotherapy groups (Supplementary Fig. 6A). Immunofluorescence revealed that radiation treatment significantly increased phosphorylated ATM expression of CT26 and MC38 cells, as well as elevated PD-L1 expression. Treatment with the ATM inhibitor not only suppressed ATM phosphorylation but also partially reduced PD-L1 expression (Supplementary Fig. 6B). Similarly, western blot analysis confirmed that inhibiting ATM kinase activity attenuated the radiation-induced upregulation of PD-L1 expression in SW480 and SW620 cells (Fig. 6A).

We investigated how ATM regulates PD-L1 expression. Specifically, we aimed to identify transcription factors that directly influence PD-L1 transcription. Among a series of classical transcription factors known to regulate PD-L1 [23], we selected those potentially dependent on ATM activation, including HIF1 [24], NF-κB [25], STAT1 [26], and STAT3 [27]. To determine the signaling pathways involved in PD-L1 regulation, we employed specific inhibitors: HIF1 inhibitor (BAY 87–2243), NF-κB inhibitor (JSH-23), STAT3 inhibitor (NSC 74859), and STAT1 inhibitor (Fludarabine), in combination with AZD0156 and IR treatment. The results showed that JSH-23 reduced IR-induced PD-L1 upregulation, producing effects similar to AZD0156 (Fig. 6B and Supplementary Fig. 6C). It suggests that activation of the NF-κB pathway may play a role in regulating PD-L1 expression. Subsequently, we further demonstrated the connection between ATM activation and both PD-L1 expression and p65-dependent NF-κB activation following radiation. Inhibition of ATM activation using AZD0156 suppressed both IR-induced activation of the NF-κB subunit p65 and the upregulation of PD-L1 expression (Fig. 6C). Moreover, we used ChIP-qPCR to examine the interaction between p65 and the PD-L1 promoter. The results showed that IR increased p65 binding to the PD-L1 promoter (as indicated by IP/input), which was effectively blocked by AZD0156 (Fig. 6D). These results suggest that the upregulation of

PD-L1 expression following IR may be partially mediated through ATM activation and subsequent p65-dependent NF-κB activation.

We then investigated how ATM activation triggers NF-κB activation. Previous studies have reported that ATM can translocate from the nucleus to the cytoplasm, where it activates the NF-κB essential modulator (NEMO) [28]. Activated ATM interacts with SUMOylated NEMO, triggering p65 nuclear translocation and NF-κB activation [28,29]. To investigate whether the radiation-induced upregulation of PD-L1 expression in CRC cells is mediated by the ATM-NEMO interaction and subsequent NF-κB activation, we performed co-immunoprecipitation (co-IP) experiments. Immunoprecipitation (IP) using an ATM antibody followed by immunoblotting (IB) to detect NEMO revealed colocalization between ATM and NEMO after irradiation, and colocalization increased with higher radiation doses (Fig. 6E, upper panel). Similarly, IP with a NEMO antibody in irradiated cells also confirmed the interaction between ATM and NEMO (Fig. 6E, lower panel). We then validated whether the interaction between ATM and NEMO depends on ATM activation. The results showed that treatment with AZD0156 reduced the IR-induced colocalization of ATM and NEMO (Fig. 6F, upper panel). As NEMO-associated ATM can be recognized by the phospho-Ser1981 ATM antibody [11,28], we performed IP with a NEMO antibody followed by IB with a phospho-Ser1981 ATM antibody. The results confirmed that AZD0156 significantly reduced the interaction between NEMO and activated ATM (Fig. 6F, lower panel), providing further evidence that the ATM-NEMO interaction is dependent on ATM kinase activity.

Since high PD-L1 expression and immune infiltration correlate with ICI responsiveness in advanced non-small cell lung cancer [30], we treated tumor-bearing mice with an anti-mouse PD-L1 antibody (αPD-L1) to evaluate combined treatment efficacy. Mice with implanted CT26 cells were grouped into four treatment regimens: (i) Radiation alone (IR); (ii) Radiation + anti-PD-L1 treatment (IR + αPD-L1); (iii) AZD0156 + radiation (IR + AZD); and (iv) AZD0156 + radiation + anti-PD-L1 treatment (IR + AZD + αPD-L1) (Supplementary Fig. 7A). Results showed that combining αPD-L1 with radiation and AZD0156 significantly suppressed tumor growth (Supplementary Fig. 7B), achieving a tumor regression rate of 71.4 % in the triple therapy group (Supplementary Fig. 7C). We evaluated the toxicity of the triple therapy and found that while both radiotherapy combined with AZD0156 (dual therapy) and radiotherapy combined with AZD0156 and anti-PD-L1 (triple therapy) caused temporary weight loss in mice, the reduction was acceptable (<20 %) and recovered within 3–4 weeks (Supplementary Fig. 7D). Serum levels of AST and ALT before, during, and after treatment showed no significant differences between groups and remained normal (Supplementary Fig. 7E). Moreover,

---

Fig. 6. Triple therapy combining radiotherapy, AZD0156, and anti-PD-L1 blockade significantly enhances antitumor activity. **A.** Western blot analysis was performed to detect PD-L1 protein expression in cells treated with control, IR alone (6 Gy), or IR combined with AZD0156 (1 uM, 2 uM). **B.** The SW480 cells were divided into non-IR and IR groups. The IR group underwent either no treatment or treatment with various inhibitors, including Bay11-2243 (10 uM), NSC 74859 (100 uM), fludarabine (20 uM), JSH-23 (10 uM), AZD0156 (4 uM). PD-L1 expression was analyzed by flow cytometry 48 h post-IR. **C.** SW480 and SW620 cells were treated with control, IR alone (6 Gy), or IR combined with AZD0156 (1 uM, 2 uM). Total and phosphorylated levels of ATM, p65, and PD-L1 were analyzed by western blot 48 h post-treatment. **D.** ChIP-qPCR analysis of p65 occupancy on the PD-L1 promoter in SW480 and SW620 cells treated with control, IR alone (6 Gy), IR combined with AZD0156 (4 uM). Data are presented as fold enrichment relative to the input. **E.** SW480 and SW620 cells were treated with ionizing radiation (IR) at doses of 0 Gy, 6 Gy, and 12 Gy, and protein lysates were collected 8 h post-treatment. The interaction between ATM and NEMO was evaluated using co-IP assays. Upper panel: IP was performed using an anti-ATM mouse monoclonal antibody, followed by IB with an anti-NEMO rabbit polyclonal antibody. Lower panel: IP was performed using an anti-NEMO rabbit polyclonal antibody, followed by IB with an anti-ATM mouse monoclonal antibody. **F.** SW480 and SW620 cells were treated with a control, IR alone (6 Gy), or IR in combination with AZD0156 (2 uM, 4 uM). The interaction between ATM and NEMO was analyzed by co-IP, including IP with anti-ATM followed by IB with anti-NEMO, and IP with anti-NEMO followed by IB with anti-Phospho-ATM (S1981) mouse monoclonal antibody. **G.** Schematic of subcutaneous MC38 tumors (100–300 mm³) in grown in C57BL/6J mice. Mice were treated with IR (5 Gy × 3), IR with anti-PD-L1 (200 ug), IR with AZD0156 (10 mg/kg) or IR with anti-PD-L1 plus AZD0156. **H.** Waterfall plot showing the tumor growth rate for individual mice. **I.** Kaplan-Meier survival curves of mice were shown. **J.** Response to treatment was reflected by tumor growth curves from each individual mouse. **K.** Experimental design of efficacy study in mice with large tumors (300–600 mm³). Mice were treated with IR (8 Gy × 3), IR with anti-PD-L1 (200 ug), IR with AZD0156 (10 mg/kg) or IR with anti-PD-L1 plus AZD0156. **L.** Waterfall plot showing the tumor growth rate for individual mice. **M.** Kaplan-Meier survival curves of mice in each group. **N.** Tumor growth curves of each individual mouse subjected to different treatments. Data are represented as mean ± SEM. *p < 0.05, **p < 0.01, ***p < 0.001, ****p < 0.0001.

CKMB and TNT levels were normal, with no abnormalities detected (Supplementary Fig. 7F). HE staining of myocardial tissue three weeks post-treatment also revealed no cardiac injury (Supplementary Fig. 7G). The triple therapy effectively inhibited tumor growth without significant weight loss or additional liver or cardiac toxicity in mice. We validated the triple therapy's efficacy in a subcutaneous tumor model in C57 mice using MC38 cells (Fig. 6G). Radiation combined with AZD0156 showed limited effectiveness in tumor control, but the addition of αPD-L1 significantly improved outcomes, with 60 % of tumors regressing (Fig. 6H and 6 J). Survival data confirmed no mortality in the triple therapy group during the observation period (Fig. 6I).

We targeted large tumors, known for their rapid growth and poor response to treatment [31,32]. In a large tumor-bearing mouse model (>300 mm^3), treatment is particularly challenging due to the tumors' rapid growth [31]. Therefore, we used a subcutaneous MC38 tumor model, grouping mice when the tumor volume reached 300–600 mm^3 (Fig. 6K). We modified the treatment protocol by increasing the radiation dose to 8 Gy and adding two cycles of anti-PD-L1 antibody. This approach induced tumor regression, with a complete remission rate of 66.7 % in the triple therapy group (Fig. 6L and 6 N). Survival data showed no mortality in this group (Fig. 6M). The mortality rates for mice with large tumors treated solely with radiation were 66.7 %, and those treated with radiation combined with anti-PD-L1 were 33.3 %. In contrast, mice with medium-sized tumors (100–300 mm^3) treated with triple regimens had a mortality rate of 100 %, indicating that our modified treatment significantly improved survival benefits. No significant weight loss occurred in any treatment group (Supplementary Fig. 7H). Combining the ATM inhibitor with radiation and ICI effectively controlled growth in large, treatment-resistant tumors. The triple therapy significantly improved remission rates and survival in mice with high tumor burdens..

Discussion

It is projected that by the next decade, a growing proportion of individuals under 50 years old will be diagnosed with rectal cancer (25 %) and colon cancer (12 %) [33]. Early-onset colorectal cancer patients often present with advanced tumors at diagnosis, missing the optimal window for surgical intervention [33,34]. While radiotherapy is the standard treatment for locally advanced rectal cancer, it is also an effective option for advanced CRC, particularly for younger patients with lower rectal cancer who prioritize sphincter preservation [35]. However, poor tumor response to radiation can result in insufficient regression, reduced surgical options, and tumor recurrence, severely compromising quality of life and increasing disease burden [36].

The DNA damage response (DDR) pathway is a key mechanism activated under radiation stress, and its role in damage repair contributes to radiation resistance [3]. ATM is a central molecule in the DDR pathway, primarily responsible for repairing double-strand DNA breaks [4]. However, whether ATM plays additional roles or interacts with other signaling pathways following radiation remains an area for further investigation. Our analysis of rectal cancer clinical samples revealed that radiotherapy fosters ATM kinase activation, with high levels of phosphorylated ATM correlating with poor radiotherapy response. Both in vitro and in vivo experiments confirmed that radiation significantly activates ATM in CRC cells, raising phosphorylation levels. Currently, clinical-grade ATM inhibitors are limited, with AZD0156, a selective oral ATM inhibitor, undergoing early clinical trials [37,38]. Our findings suggest that while AZD0156 has minimal impact on CRC tumor growth alone, it substantially enhances tumor radiosensitivity in vitro and in vivo. Importantly, AZD0156 not only inhibits

post-radiation tumor cell growth but also enhances anti-tumor immunity, contributing to effective tumor suppression. Thus, AZD0156 holds potential as a tumor radiosensitizer. Moreover, ATM mutations or deletions, which disrupt DNA damage repair, lead to increased genetic instability and are associated with various cancers [39]. Although ATM mutation frequency in CRC patients stands at only about 9–15 % [40] (Supplementary Fig. 7I), combining ATM inhibitors with radiotherapy shows promise for improving clinical outcomes. Additionally, ATM inhibitors like AZD0156 have demonstrated synergistic effects in preclinical studies when combined with drugs such as olaparib, EGFR inhibitors, and irinotecan, suggesting potential for combining ATM inhibitors with cytotoxic therapies in anti-tumor strategies. Furthermore, phosphorylated ATM could serve as a biomarker for predicting radiotherapy efficacy and guiding the design of combined treatments involving ATM inhibitors.

Elevated ROS levels, a hallmark of oxidative stress, contribute significantly to radiation-induced cell death [6]. Cells from Ataxia Telangiectasia (A-T) patients and ATM-deficient mice show heightened intracellular ROS levels and increased sensitivity to oxidative stress [41]. However, the impact of ATM inhibition on ROS levels after radiation remains unclear. Our research demonstrates that inhibiting ATM activation increases ROS levels in tumors post-radiation. Elevated ROS can damage the mitochondrial electron transport chain and impair the mitochondrial antioxidant system, leading to higher mitochondrial ROS levels. As the primary sites of ROS production, damaged mitochondria generate more ROS, creating a self-perpetuating cycle. Additionally, we observed increased autophagosomes in cells following radiation. Enhanced autophagy reduces cell apoptosis, clears damaged mitochondria, and decreases ROS accumulation, thereby maintaining redox balance [42]. Our results indicate that inhibiting radiation-induced ATM activation disrupts the ROS balance controlled by the ATM/CHK2/Beclin 1/autophagy pathway, consistent with findings by Guo et al. [21]. Our studies show that post-radiation, ATM inhibitors elevate mitochondrial ROS levels and cause mitochondrial damage, leading to cytoplasmic leakage of mitochondrial DNA.

Beyond directly damaging tumor cells, radiation induces biological effects that promote antitumor immune responses. It is well-established that radiotherapy-induced micronuclei with compromised membranes trigger cGAS recognition of micronuclear DNA, activating the STING-type I IFN pathway [16]. Our research identifies an additional pathway for immune recognition, where ATM inhibition enhances mitochondrial damage post-radiation, promoting the release of mitochondrial DNA into the cytoplasm and activating the STING pathway. This provides new insights into the relationship between tumor cell damage and the initiation of innate immune recognition. Radiation plays a dual role in regulating the tumor immune microenvironment. While it fosters CD8+ T cell infiltration and activation and antigen presentation [14], it also triggers DDR signaling, upregulating PD-L1 expression in cancer cells [43]. Radiation-induced PD-L1 upregulation hampers antitumor immune activation. In prostate cancer cells, ATM activation enhances paclitaxel-induced PD-L1 expression [44], and in glioma cells, PD-L1 upregulation after radiation depends on ATM/ATR/Chk1 activation [45]. However, the role of ATM in regulating PD-L1 expression after radiation has not been well studied in CRC. In our studies, the ATM inhibitor AZD0156 alleviated radiation-induced PD-L1 upregulation in CRC cells. Through inhibitor screening to identify potential pathways regulating ATM-mediated PD-L1 expression, we found that radiation-induced upregulation of PD-L1 expression may be associated with the activation of the NFκB pathway. Previous studies have suggested that under stress conditions, a portion of activated ATM is exported from the nucleus to the cytoplasm in a NEMO-dependent manner [28]. The phosphorylated ATM and SUMOylated NEMO can bind to each other, promot-

ing NFκB activation [29]. Our study confirms that radiation promotes the ATM-NEMO interaction, which can be blocked by AZD0156, indicating that this interaction is kinase activity-dependent.

Overcoming the intrinsic resistance to immune checkpoint blockade (ICI) in microsatellite stable (MSS) colorectal cancer remains a significant clinical challenge [22]. To address this, strategies combining radiotherapy and immunotherapy are actively being explored. However, most studies on preoperative radiotherapy combined with immunotherapy for locally advanced rectal cancer show limited efficacy, with pathological complete response (pCR) rates ranging from 20 % to 30 % [46]. Similarly, for advanced metastatic colorectal cancer, the overall response rate (ORR) for dual immune checkpoint inhibitors combined with radiotherapy is suboptimal (8 %-15 %) [47]. Therefore, there is an urgent need to explore novel combination strategies to enhance tumor sensitivity to ICI. Our study investigated the therapeutic effect of a "radiotherapy combined with ATM inhibitor AZD0156 and anti-PD-L1" triplet strategy. The results showed that this triplet therapy significantly promoted tumor regression and extended survival in the mouse model.

Baseline tumor size is also a key prognostic factor affecting the efficacy of ICI therapy in various cancers, with larger tumors often correlating with poorer treatment outcomes [48,49]. In this study, we developed a large tumor model to evaluate its response to the triplet therapy. Remarkably, the triplet therapy achieved excellent tumor control in the large tumor model, with 67 % of tumors showing complete remission in the mouse model.

ATM inhibitors not only enhance radiation-induced tumor cell death but also promote immune microenvironment activation triggered by radiation. Additionally, they partially counteract the immunosuppressive effects of PD-L1 upregulation. As a result, combining radiotherapy with ATM inhibitors and PD-L1 blockade represents a promising synergistic strategy for effective cancer treatment.

Conclusion

In conclusion, our study emphasizes the importance of targeting radiation-induced ATM activation to enhance radiosensitivity in colorectal cancer (CRC). Inhibition of ATM with AZD0156 increases cell radiosensitivity, reduces tumor growth, and boosts anti-tumor immunity. Mechanistically, ATM inhibition promotes the accumulation of ROS and mitochondrial damage, activating cytoplasmic mtDNA-induced STING type-I IFN signaling, which leads to cell death and an immune-activating microenvironment (Graphical Abstract). Additionally, AZD0156 inhibits NFκB activation, reducing radiation-induced PD-L1 upregulation and potentially overcoming immunosuppressive barriers. These promising preclinical results suggest that combining radiotherapy with ATM inhibitors and immune checkpoint blockade may provide an effective strategy to improve CRC outcomes. This approach warrants further clinical exploration to enhance therapeutic efficacy and overcome resistance.

Declaration of competing interest

The authors declare that they have no known competing financial interests or personal relationships that could have appeared to influence the work reported in this paper.

Acknowledgments

Appendix A. Supplementary data

Supplementary data to this article can be found online at https://doi.org/10.1016/j.jare.2024.12.023.

References

[1] Bray F, Laversanne M, Sung H, Ferlay J, Siegel RL, Soerjomataram I, et al. Global cancer statistics 2022: GLOBOCAN estimates of incidence and mortality worldwide for 36 cancers in 185 countries. CA Cancer J Clin 2024;74:229–63. doi: https://doi.org/10.3322/caac.21834.

[2] Alese OB, Zhou W, Jiang R, Zakka K, Huang Z, Okoli C, et al. Predictive and prognostic effects of primary tumor size on colorectal cancer survival. Front Oncol 2021;11.

[3] Goldstein M, Kastan MB. The DNA damage response: implications for tumor responses to radiation and chemotherapy. Annu Rev Med 2015;66:129–43. doi: https://doi.org/10.1146/annurev-med-081313-121208.

[4] Jin MH, Oh D-Y. ATM in DNA repair in cancer. Pharmacol Ther 2019;203:. doi: https://doi.org/10.1016/j.pharmthera.2019.07.002107391.

[5] Pike KG, Barlaam B, Cadogan E, Campbell A, Chen Y, Colclough N, et al. The identification of potent, selective, and orally available inhibitors of ataxia telangiectasia mutated (ATM) kinase: the discovery of AZD0156 (8-{6-[3-(Dimethylamino)propoxy]pyridin-3-yl}-3-methyl-1-(tetrahydro-2H-pyran-4-yl)-1,3-dihydro-2H-imidazo[4,5-c]quinolin-2-one). J Med Chem 2018;61:3823–41. doi: https://doi.org/10.1021/acs.jmedchem.7b01896.

[6] Srinivas US, Tan BWQ, Vellayappan BA, Jeyasekharan AD. ROS and the DNA damage response in cancer. Redox Biol 2019;25:. doi: https://doi.org/10.1016/j.redox.2018.101084101084.

[7] da Costa AABA, Chowdhury D, Shapiro GI, D'Andrea AD, Konstantinopoulos PA. Targeting replication stress in cancer therapy. Nat Rev Drug Discov 2022:1–21. doi: https://doi.org/10.1038/s41573-022-00558-5.

[8] Chabanon RM, Muirhead G, Krastev DB, Adam J, Morel D, Garrido M, et al. PARP inhibition enhances tumor cell-intrinsic immunity in ERCC1-deficient non-small cell lung cancer. J Clin Invest 2019;129:1211–28. doi: https://doi.org/10.1172/JCI123319.

[9] Fang Y, Zhan Y, Xie Y, Du S, Chen Y, Zeng Z, et al. Integration of glucose and cardiolipin anabolism confers radiation resistance of HCC. Hepatology 2021. doi: https://doi.org/10.1002/hep.32177.

[10] Li J-Y, Zhao Y, Gong S, Wang M-M, Liu X, He Q-M, et al. TRIM21 inhibits irradiation-induced mitochondrial DNA release and impairs antitumour immunity in nasopharyngeal carcinoma tumour models. Nat Commun 2023;14:865. doi: https://doi.org/10.1038/s41467-023-36523-y.

[11] Bakkenist CJ, Kastan MB. DNA damage activates ATM through intermolecular autophosphorylation and dimer dissociation. Nature 2003;421:499–506. doi: https://doi.org/10.1038/nature01368.

[12] Biddlestone-Thorpe L, Sajjad M, Rosenberg E, Beckta JM, Valerie NCK, Tokarz M, et al. ATM kinase inhibition preferentially sensitizes p53-mutant glioma to ionizing radiation. Clin Cancer Res 2013;19:3189–200. doi: https://doi.org/10.1158/1078-0432.CCR-12-3408.

[13] Parikh AR, Szabolcs A, Allen JN, Clark JW, Wo JY, Raabe M, et al. Radiation therapy enhances immunotherapy response in microsatellite stable colorectal and pancreatic adenocarcinoma in a phase II trial. Nat Cancer 2021;2:1124–35. doi: https://doi.org/10.1038/s43018-021-00269-7.

[14] Zhang Z, Liu X, Chen D, Yu J. Radiotherapy combined with immunotherapy: the dawn of cancer treatment. Signal Transduct Target Ther 2022;7:258. doi: https://doi.org/10.1038/s41392-022-01102-y.

[15] Sheng H, Huang Y, Xiao Y, Zhu Z, Shen M, Zhou P, et al. ATR inhibitor AZD6738 enhances the antitumor activity of radiotherapy and immune checkpoint inhibitors by potentiating the tumor immune microenvironment in hepatocellular carcinoma. J Immunother Cancer 2020;8:. doi: https://doi.org/10.1136/jitc-2019-000340e000340.

[16] McLaughlin M, Patin EC, Pedersen M, Wilkins A, Dillon MT, Melcher AA, et al. Inflammatory microenvironment remodelling by tumour cells after radiotherapy. Nat Rev Cancer 2020;20:203–17. doi: https://doi.org/10.1038/s41568-020-0246-1.

[17] Härtlova A, Erttmann SF, Raffi FAM, Schmalz AM, Resch U, Anugula S, et al. DNA damage primes the type I interferon system via the cytosolic DNA sensor STING to promote anti-microbial innate immunity. Immunity 2015;42:332–43. doi: https://doi.org/10.1016/j.immuni.2015.01.012.

[18] Yamazaki T, Kirchmair A, Sato A, Buqué A, Rybstein M, Petroni G, et al. Mitochondrial DNA drives abscopal responses to radiation that are inhibited by autophagy. Nat Immunol 2020;21:1160–71. doi: https://doi.org/10.1038/s41590-020-0751-0.

[19] Kim GJ, Fiskum GM, Morgan WF. A role for mitochondrial dysfunction in perpetuating radiation-induced genomic instability. Cancer Res 2006;66:10377–83. doi: https://doi.org/10.1158/0008-5472.CAN-05-3036.

[20] Li X, Fang F, Gao Y, Tang G, Xu W, Wang Y, et al. ROS induced by KillerRed targeting mitochondria (mtKR) Enhances apoptosis caused by radiation via Cyt c/caspase-3 pathway. Oxid Med Cell Longev 2019;2019:. doi: https://doi.org/10.1155/2019/4528616 4528616.

[21] Guo Q-Q, Wang S-S, Zhang S-S, Xu H-D, Li X-M, Guan Y, et al. ATM-CHK2-Beclin 1 axis promotes autophagy to maintain ROS homeostasis under oxidative stress. EMBO J 2020;39:. doi: https://doi.org/10.15252/embj.2019103111 e103111.

[22] Cai L, Chen A, Tang D. A new strategy for immunotherapy of microsatellite-stable (MSS)-type advanced colorectal cancer: Multi-pathway combination therapy with PD-1/PD-L1 inhibitors. Immunology 2024;173:209–26. doi: https://doi.org/10.1111/imm.13785.

[23] Yamaguchi H, Hsu J-M, Yang W-H, Hung M-C. Mechanisms regulating PD-L1 expression in cancers and associated opportunities for novel small-molecule therapeutics. Nat Rev Clin Oncol 2022;19:287–305. doi: https://doi.org/10.1038/s41571-022-00601-9.

[24] Shi Y, Liu Z, Zhang Q, Vallee I, Mo Z, Kishi S, et al. Phosphorylation of seryl-tRNA synthetase by ATM/ATR is essential for hypoxia-induced angiogenesis. PLoS Biol 2020;18. doi: https://doi.org/10.1371/journal.pbio.3000991. e3000991.

[25] Cho E-A, Kim E-J, Kwak S-J, Juhnn Y-S. cAMP signaling inhibits radiation-induced ATM phosphorylation leading to the augmentation of apoptosis in human lung cancer cells. Mol Cancer 2014;13:36. doi: https://doi.org/10.1186/1476-4598-13-36.

[26] Deng S, Wang J, Hu Y, Sun Y, Yang X, Zhang B, et al. Irradiated tumour cell-derived microparticles upregulate MHC-I expression in cancer cells via DNA double-strand break repair pathway. Cancer Lett 2024;592:. doi: https://doi.org/10.1016/j.canlet.2024.216898 216898.

[27] Tian Y, Liu C, Li Z, Ai M, Wang B, Du K, et al. Exosomal B7-H4 from irradiated glioblastoma cells contributes to increase FoxP3 expression of differentiating Th1 cells and promotes tumor growth. Redox Biol 2022;56:. doi: https://doi.org/10.1016/j.redox.2022.102454 102454.

[28] Wu Z-H, Shi Y, Tibbetts RS, Miyamoto S. Molecular linkage between the kinase ATM and NF-kappaB signaling in response to genotoxic stimuli. Science 2006;311:1141–6. doi: https://doi.org/10.1126/science.1121513.

[29] Wuerzberger-Davis SM, Nakamura Y, Seufzer BJ, Miyamoto S. NF-kappaB activation by combinations of NEMO SUMOylation and ATM activation stresses in the absence of DNA damage. Oncogene 2007;26:641–51. doi: https://doi.org/10.1038/sj.onc.1209815.

[30] Sun D, Liu J, Zhou H, Shi M, Sun J, Zhao S, et al. Classification of tumor immune microenvironment according to programmed death-ligand 1 expression and immune infiltration predicts response to immunotherapy plus chemotherapy in advanced patients with NSCLC. J Thorac Oncol 2023. doi: https://doi.org/10.1016/j.jtho.2023.03.012.

[31] Liu Y, Tang P, Xiao P, Luo S, Zhang S, Zhang H, et al. Molecular stacking composite nanoparticles of gossypolone and thermodynamic agent for elimination of large tumor in mice via electrothermal-thermodynamic-chemo trimodal combination therapy. Adv Funct Mater 2022;32:. doi: https://doi.org/10.1002/adfm.2022016662201666.

[32] Morita-Tokuhiro S, Ogawa Y, Yokota N, Tsuzuki A, Oda H, Ishida N, et al. Development of a novel enzyme-targeting radiosensitizer (New KORTUC) using a gelatin-based hydrogel instead of a sodium hyaluronate. Cancers (Basel) 2016;8:E10. doi: https://doi.org/10.3390/cancers8010010.

[33] Sinicrope FA. Increasing incidence of early-onset colorectal cancer. N Engl J Med 2022;386:1547–58. doi: https://doi.org/10.1056/NEJMra2200869.

[34] You YN, Xing Y, Feig BW, Chang GJ, Cormier JN. Young-onset colorectal cancer: is it time to pay attention? Arch Intern Med 2012;172:287–9. doi: https://doi.org/10.1001/archinternmed.2011.602.

[35] Custers PA, van der Sande ME, Grotenhuis BA, Peters FP, van Kuijk SMJ, Beets GL, et al. Long-term quality of life and functional outcome of patients with rectal cancer following a watch-and-wait approach. JAMA Surg 2023;158:. doi: https://doi.org/10.1001/jamasurg.2023.0146 e230146.

[36] Huang R-X, Zhou P-K. DNA damage response signaling pathways and targets for radiotherapy sensitization in cancer. Signal Transduct Target Ther 2020;5:60. doi: https://doi.org/10.1038/s41392-020-0150-x.

[37] Davis SL, Hartman SJ, Bagby SM, Schlaepfer M, Yacob BW, Tse T, et al. ATM kinase inhibitor AZD0156 in combination with irinotecan and 5-fluorouracil in preclinical models of colorectal cancer. BMC Cancer 2022;22:1107. doi: https://doi.org/10.1186/s12885-022-10084-7.

[38] Riches LC, Trinidad AG, Hughes G, Jones GN, Hughes AM, Thomason AG, et al. Pharmacology of the ATM inhibitor AZD0156: potentiation of irradiation and olaparib responses preclinically. Mol Cancer Ther 2020;19:13–25. doi: https://doi.org/10.1158/1535-7163.MCT-18-1394.

[39] Savitsky K, Bar-Shira A, Gilad S, Rotman G, Ziv Y, Vanagaite L, et al. A single ataxia telangiectasia gene with a product similar to PI-3 kinase. Science 1995;268:1749–53. doi: https://doi.org/10.1126/science.7792600.

[40] Zhou P, Wu X, Chen H, Hu Y, Zhang H, Wu L, et al. The mutational pattern of homologous recombination-related (HRR) genes in Chinese colon cancer and its relevance to immunotherapy responses. Aging (Albany NY) 2020;13:2365–78. doi: https://doi.org/10.18632/aging.202267.

[41] Lee J-H, Paull TT. Cellular functions of the protein kinase ATM and their relevance to human disease. Nat Rev Mol Cell Biol 2021;22:796–814. doi: https://doi.org/10.1038/s41580-021-00394-2.

[42] Filomeni G, De Zio D, Cecconi F. Oxidative stress and autophagy: the clash between damage and metabolic needs. Cell Death Differ 2015;22:377–88. doi: https://doi.org/10.1038/cdd.2014.150.

[43] Deng L, Liang H, Burnette B, Beckett M, Darga T, Weichselbaum RR, et al. Irradiation and anti-PD-L1 treatment synergistically promote antitumor immunity in mice. J Clin Invest 2014;124:687–95. doi: https://doi.org/10.1172/JCI67313.

[44] Wang Z, Zhang X, Li W, Su Q, Huang Z, Zhang X, et al. ATM/NEMO signaling modulates the expression of PD-L1 following docetaxel chemotherapy in prostate cancer. J Immunother Cancer 2021;9:. doi: https://doi.org/10.1136/jitc-2020-001758 e001758.

[45] Permata TBM, Sato H, Gu W, Kakoti S, Uchihara Y, Yoshimatsu Y, et al. High linear energy transfer carbon-ion irradiation upregulates PD-L1 expression more significantly than X-rays in human osteosarcoma U2OS cells. J Radiat Res 2021;62:773–81. doi: https://doi.org/10.1093/jrr/rrab050.

[46] Wang Y, Shen L, Wan J, Zhang H, Wu R, Wang J, et al. Neoadjuvant chemoradiotherapy combined with immunotherapy for locally advanced rectal cancer: A new era for anal preservation. Front Immunol 2022;13:. doi: https://doi.org/10.3389/fimmu.2022.1067036 1067036.

[47] Lin Z, Cai M, Zhang P, Li G, Liu T, Li X, et al. Phase II, single-arm trial of preoperative short-course radiotherapy followed by chemotherapy and camrelizumab in locally advanced rectal cancer. J Immunother Cancer 2021;9:. doi: https://doi.org/10.1136/jitc-2021-003554 e003554.

[48] Hopkins AM, Kichenadasse G, McKinnon RA, Rowland A, Sorich MJ. Baseline tumor size and survival outcomes in lung cancer patients treated with immune checkpoint inhibitors. Semin Oncol 2019;46:380–4. doi: https://doi.org/10.1053/j.seminoncol.2019.10.002.

[49] Joseph RW, Elassaiss-Schaap J, Kefford R, Hwu W-J, Wolchok JD, Joshua AM, et al. Baseline tumor size is an independent prognostic factor for overall survival in patients with melanoma treated with pembrolizumab. Clin Cancer Res 2018;24:4960–7. doi: https://doi.org/10.1158/1078-0432.CCR-17-2386.